A global climatology of upper-tropospheric ice supersaturation occurrence inferred from the Atmospheric Infrared Sounder calibrated by MOZAIC

N. Lamquin, C.J. Stubenrauch, K. Gierens, U. Burkhardt, H. Smit

Atmos. Chem. Phys., 12, 381–405, 2012
www.atmos-chem-phys.net/12/381/2012/
doi:10.5194/acp-12-381-2012

Atmospheric Chemistry and Physics

A global climatology of upper-tropospheric ice supersaturation occurrence inferred from the Atmospheric Infrared Sounder calibrated by MOZAIC

N. Lamquin[1], **C. J. Stubenrauch**[1], **K. Gierens**[2], **U. Burkhardt**[2], **and H. Smit**[3]

[1]Laboratoire de Météorologie Dynamique, UMR8539, CNRS/IPSL – Ecole Polytechnique, Palaiseau, France
[2]Deutsches Zentrum für Luft- und Raumfahrt, Oberpfaffenhofen, Germany
[3]Forschungzentrum Jülich, Institut für Chemie der belasteten Atmosphäre (ICG2), Jülich, Germany

Correspondence to: N. Lamquin (nicolas.lamquin@lmd.polytechnique.fr)

Received: 9 September 2010 – Published in Atmos. Chem. Phys. Discuss.: 27 April 2011
Revised: 3 September 2011 – Accepted: 12 December 2011 – Published: 5 January 2012

Abstract. Ice supersaturation in the upper troposphere is a complex and important issue for the understanding of cirrus cloud formation. On one hand, infrared sounders have the ability to provide cloud properties and atmospheric profiles of temperature and humidity. On the other hand, they suffer from coarse vertical resolution, especially in the upper troposphere and therefore are unable to detect shallow ice supersaturated layers. We have used data from the Measurements of OZone and water vapour by AIrbus in-service airCraft experiment (MOZAIC) in combination with Atmospheric InfraRed Sounder (AIRS) relative humidity measurements and cloud properties to develop a calibration method for an estimation of occurrence frequencies of ice supersaturation. This method first determines the occurrence probability of ice supersaturation, detected by MOZAIC, as a function of the relative humidity determined by AIRS. The occurrence probability function is then applied to AIRS data, independently of the MOZAIC data, to provide a global climatology of upper-tropospheric ice supersaturation occurrence. Our climatology is then compared to ice supersaturation occurrence statistics from MOZAIC alone and related to high cloud occurrence from the Cloud-Aerosol Lidar with Orthogonal Polarization (CALIOP). As an example of application it is compared to model climatologies of ice supersaturation from the Integrated Forecast System (IFS) of the European Centre for Medium-Range Weather Forecasts (ECMWF) and from the European Centre HAmburg Model (ECHAM4). This study highlights the benefits of multi-instrumental synergies for the investigation of upper tropospheric ice supersaturation.

1 Introduction

Ice supersaturation (or "ISS", relative humidity with respect to ice larger than 100 %) is a prerequisite for the nucleation of cirrus clouds (e.g. Haag et al., 2003) and for the persistence of condensation trails (Schumann, 1996). The growing necessity of a better representation of ice cloud formation processes (Waliser et al., 2009; Tompkins et al., 2007) has increased interest in the parametrization of supersaturation in climate models. While radiosondes and in situ measurements provide relative humidity at a high vertical resolution (Spichtinger et al., 2003a; Krämer et al., 2009), continuous and global observations are only achievable from satellite measurements which, in turn, suffer from a limited vertical resolution.

For example, Kahn et al. (2008) and Lamquin et al. (2008) have shown that cirrus clouds have generally a smaller vertical extent (about 2 km) than the AIRS vertical resolution (>3 km in the upper troposphere, Maddy and Barnet, 2008) and that relative humidity with respect to ice (RHi) inside cirrus clouds is difficult to determine since clear parts of the profile, over or under the clouds, are taken into account in its computation. In addition, the radiances used for the retrieval of atmospheric temperature and water vapour profiles are cloud cleared (Chahine et al., 2006) and therefore these RHi profiles correspond more to the atmosphere around the clouds. Thus RHi distributions in the presence of cirrus clouds show dry biases when compared to in situ measurements and model parametrizations (e.g. Lamquin et al., 2009).

Ice supersaturation occurs in thin layers of the atmosphere (about 500 m according to Spichtinger et al., 2003a), thus it is even harder to detect by satellites (e.g. Gierens et al., 2004). As a consequence, its global frequency of occurrence is underestimated if a threshold of 100 % is used (Gettelman et al., 2006a). Therefore, Stubenrauch and Schumann (2005) have taken the coarse vertical resolution of TOVS data into account by adjusting the threshold to 70 %.

We now propose a more sophisticated method based on the construction of an a priori knowledge of the occurrence probability of ice supersaturation inside a vertical pressure layer as a function of the AIRS relative humidity (from now onwards termed "RHi_A") computed over this vertical pressure layer.

Section 2 presents AIRS and MOZAIC datasets. Section 3 presents relationships inferred from the collocation of AIRS and MOZAIC as well as the calibration method. This method is then employed in Sect. 4, independently of the MOZAIC data, to build a climatology of ice supersaturation from the AIRS data only. ISS occurrences are compared to those obtained by MOZAIC. We further study cirrus occurrence from CALIOP in relation to ice supersaturation occurrence. As an example of further applications we present in Sect. 5 first comparisons with ISS occurrence climatologies from ECMWF and ECHAM4. Data other than AIRS and MOZAIC are briefly introduced before each comparison because the relevance of the extracted parameters then appears in a more comprehensible manner. We summarize our results in Sect. 6.

2 Data handling

2.1 AIRS data, quality and vertical resolution

On board the NASA Aqua satellite, AIRS provides very high resolution measurements of Earth emitted radiation in three spectral bands from 3.74 to 15.40 µm, using 2378 channels. Observations exist at 01:30 and 13:30 LT since May 2002. The spatial resolution of these measurements is 13.5 km at nadir. Nine AIRS measurements (3×3) correspond to one footprint of the Advanced Microwave Sounder Unit (AMSU) within which atmospheric profiles of temperature T and specific humidity q are retrieved from cloud-cleared AIRS radiances at a spatial resolution of about 40 km at nadir (Chahine et al., 2006). AIRS level 2 (L2) standard products include temperature at 28 pressure levels from 0.1 hPa to the surface and water vapour mixing ratios w within 14 pressure layers from 50 hPa to the surface (Susskind et al., 2003, 2006). We investigate ISS occurrence within the 6 standard pressure layers 100–150, 150–200, 200–250, 250–300, 300–400, and 400–500 hPa. These layers are about 2 km thick.

Version 5 of AIRS L2 data provide quality flags for each atmospheric profile (Susskind et al., 2006; Tobin et al., 2006). We derive relative humidity RHi_A as in Lamquin et al. (2009) from profiles of best and good quality using the conditions $Qual\_H_2O \neq 2$ and $PGood > 600$ hPa. These correspond to about 70 % of all situations.

Humidity measurements for which the water vapour content is lower than 10–20 ppmv are below the nominal instrument sensitivity and are subject to a higher uncertainty (Gettelman et al., 2004). On the A-Train, the synergy of AIRS and the Microwave Limb Sounder (MLS) allows comparisons, quality evaluations and profile complementarity in the upper troposphere/lower stratosphere (UTLS) region (e.g. Fetzer et al., 2008; Liang et al., 2011). Fetzer et al. (2008) show that AIRS moisture data at altitudes higher than 200 hPa may lead to misleading results. As a consequence, RHi_A may not be fully exploitable at pressure levels higher than 200 hPa. This level is a realistic limitation to be confident in the final ISS statistics of Sect. 4. In Montoux et al. (2009) data higher than 200 hPa in altitude have shown consistency with in-situ measurements in the tropics and subtropics. Nevertheless, these authors insist on the strong influence of the a priori profiles used in the retrieval at such altitudes. We decide to include our results at such altitudes (pressure layers 100–150 and 150–200 hPa) as they show reasonable behaviours. Caution warnings recall the reader's attention throughout the analysis so that these results are not taken with too much confidence. Also, no sensitivity threshold is used to remove low values of water vapor as it would certainly lead to even more biased results then by considering all data.

2.2 AIRS-LMD cloud properties

Tu study the situations for which ISS can be determined by AIRS, we use AIRS cloud properties retrieved at LMD (Stubenrauch et al., 2010). Cloud pressure p_{cld} and IR emissivity ϵ_{cld} are determined for each AIRS footprint at the spatial scale of about 13.5 km over the period from 2003 to 2009. These parameters thus allow a distinction between no clouds in the upper troposphere (clear sky, low-level, midlevel cloudiness) and cloudiness in the upper troposphere of different optical depth (distinguished according to cloud emissivity as high opaque clouds ($\epsilon_{cld} > 0.95$), cirrus ($0.95 > \epsilon_{cld} > 0.5$) and thin cirrus ($0.5 > \epsilon_{cld}$)). The global coverage of the latter is about 2.3, 10.9 and 8.5 %, respectively.

However, by considering only situations with atmospheric profiles retrieved with good quality, their fractions change to 0.1, 4.6 and 10.3 %, respectively. Combining all seasons, Table 1 illustrates the scene dependency of statistics with which ISS can be determined. We observe that in general the average cloud emissivity is smaller for atmospheric profiles of good quality. High clouds for which AIRS provides atmospheric profiles of good quality consist of all thin cirrus and of half of the cirrus category. In the following, we use the general term "cirrus", including both categories, except in Sect. 3.3, where we distinguish between both categories.

Table 1. AIRS cloud type frequencies and average emissivities (in brackets) for atmospheric profiles with good quality data ("good") and for all data ("any"), separately over the globe ("Glb"), tropics ("Trp") and Northern Hemisphere midlatitudes ("NH"). All seasons combined.

Type/quality	(Glb) good	(Glb) any	(Trp) good	(Trp) any	(NH) good	(NH) any
High opaque clouds	0.1 (0.81)	2.3 (0.96)	0.1 (0.77)	3.4 (0.95)	0.1 (0.82)	2.6 (0.96)
Cirrus	4.6 (0.62)	10.9 (0.74)	6.3 (0.61)	15.2 (0.73)	6.0 (0.63)	13.5 (0.75)
Thin cirrus	10.3 (0.33)	8.5 (0.34)	19.4 (0.29)	17.3 (0.30)	9.7 (0.39)	8.0 (0.39)
Lmclds	37.4 (0.69)	40.5 (0.75)	19.0 (0.61)	19.2 (0.66)	48.5 (0.66)	49.3 (0.72)
Clear	47.6 (0.10)	37.8 (0.10)	55.2 (0.10)	44.9 (0.09)	35.7 (0.14)	26.6 (0.13)

Table 2. Frequency for which atmospheric profiles are of good quality within each AIRS cloud type. All regions and all seasons combined.

Cloud type	Relative frequency of good quality data
High opaque clouds	10.4
Cirrus	23.4
Thin cirrus	79.5
Thin middle clouds	89.4
Middle clouds	38.5
Thin low clouds	92.6
Low clouds	68.9
Clear	78.0

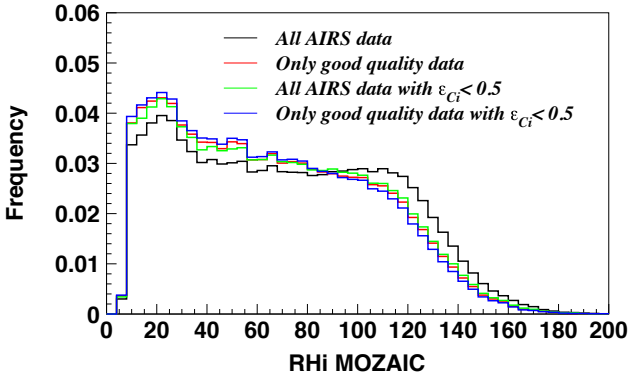

Fig. 1. Distributions of relative humidity seen from MOZAIC RHi_M in collocation with AIRS data (all qualities combined) or only with good quality AIRS data for all cloud types and when removing the thickest cirrus clouds with $\epsilon_{cld} > 0.5$.

When computing ice supersaturation occurrences in Sect. 4.2 we will only use good quality data. As cloudiness is one main limitation for retrieving profiles, the statistical distribution of the AIRS cloud types is different when considering either all data or only good quality data. This may lead to a possible bias in the ISS statistics induced by the selection of peculiar profiles. Table 2 shows the relative frequency of good quality data among each AIRS cloud type, which decreases with cloud emissivity.

To estimate further the effect of the data selection on the relative humidity, we use AIRS-MOZAIC collocated data (see Sects. 2.3 and 2.4). Figure 1 presents the distributions of MOZAIC relative humidity for cases with AIRS atmospheric profiles of good quality and for all AIRS data either for all cloudiness situations or after removing the thickest cirrus clouds ($\epsilon_{cld} > 0.5$).

The distribution corresponding to all situations is supposed to represent the "true" distribution of the upper tropospheric relative humidity. When considering only AIRS atmospheric profiles of good quality this "truth" is influenced by the removing of most of the optically thick cirrus. This indeed leads to a slightly drier distribution which means that ice supersaturation occurrence ISS_p will be slightly underestimated. However, the distribution is similar to the one of optically thin cirrus.

This comparison leads to the conclusion that for evaluating relative humidity and ISS in climate models by using AIRS observations, one has first to remove cirrus with $\epsilon_{cld} > 0.5$ in the climate model. Otherwise we expect differences in regions of high cloudiness such as the storm tracks and deep convection regions.

2.3 MOZAIC data

The MOZAIC experiment (Marenco et al., 1998) gathered concentrations of ozone and water vapour mainly in the UTLS region from measurements aboard commercial airplanes over the period August 1994–December 2007. The accuracy of the water vapour measurements is an asset for locally detecting ice supersaturation in the UTLS (Gierens et al., 1999).

However, this database only covers the main flight routes of European airliners involved in the project (Marenco et al., 1998), and it is impossible to obtain global coverage. In addition, the small amount of aircraft equipped with probing sondes as well as the randomness and the seasonal variability of flight destinations induce a non-uniform spatial and temporal representation.

Figure 2 highlights this fact for upper tropospheric data ($p_M < 500$ hPa, where p_M stands for the flight altitude) over the period 2002–2007. The top figure shows the fraction of measurements, in a $5 \times 5°$ grid, taken in summer compared

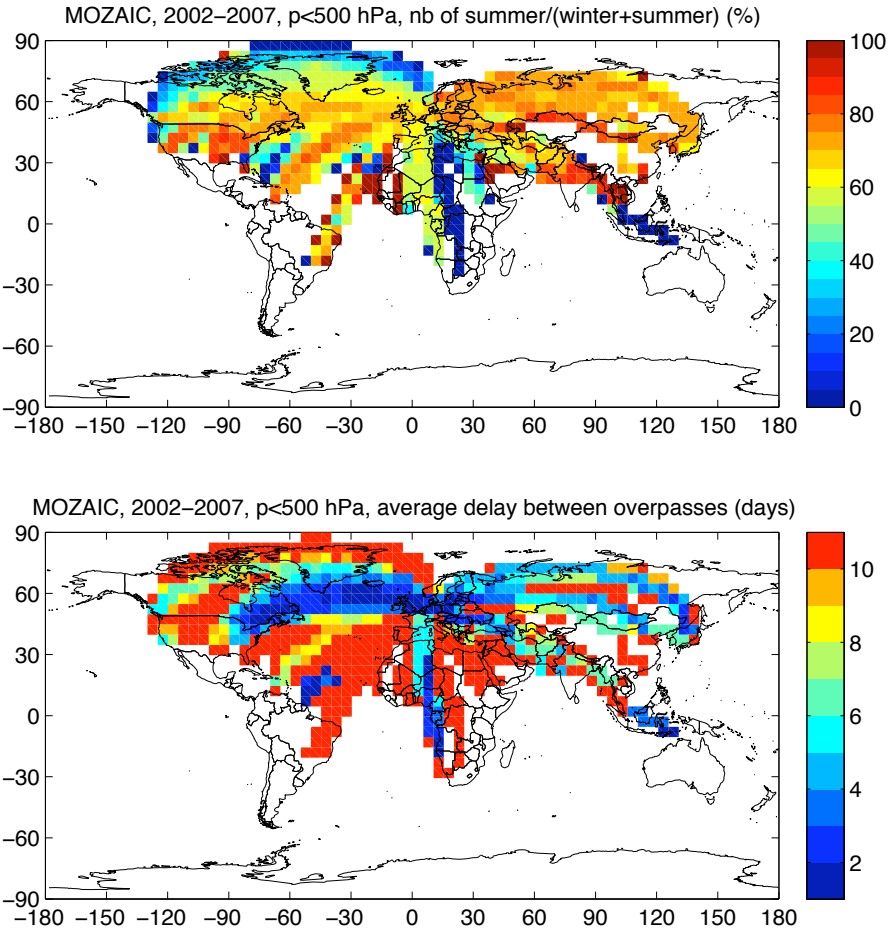

Fig. 2. Top: ratio of MOZAIC measurements taken in summer compared to the winter plus summer statistics. Bottom: average delay (in days) between two overpasses by MOZAIC flights.

Table 3. Statistics of AIRS-MOZAIC collocations (one MOZAIC single measurement per AIRS footprint) in the upper troposphere separately for different AIRS cloud types. In brackets relative percentage with respect to latitude bands and total.

AIRS situation	NH midlatitudes	Tropics	All events
Cirrus	163 070 (29.0 %, 14.2 % of total)	34 240 (27.3 %, 3.0 % of total)	290 354 (25.3 %)
Lmclds	242 053 (43.1 %, 21.1 % of total)	17 769 (14.2 %, 1.6 % of total)	355 399 (31.0 %)
Clear	156 750 (27.9 %, 13.7 % of total)	73 227 (58.5 %, 6.4 % of total)	500 266 (43.7 %)
All situations	561 873 (100 %, 49 % of total)	125 236 (100 %, 11 % of total)	1 146 019 (100 %)

to the statistics including winter and summer for each latitude/longitude. The very large variability indicates that these data will sometimes include more statistics from winter measurements (over the Arctic for example) or from summer measurements (over Russia for example).

Moreover, statistics in each grid box are not sampled within regular time steps. To illustrate this, the bottom figure of Fig. 2 shows the average interval (in days) between overpasses for each grid box. Except on very common routes, such as the North-Atlantic Flight Corridor, overpasses are not obtained on a daily basis. Rather, about 5 days are necessary

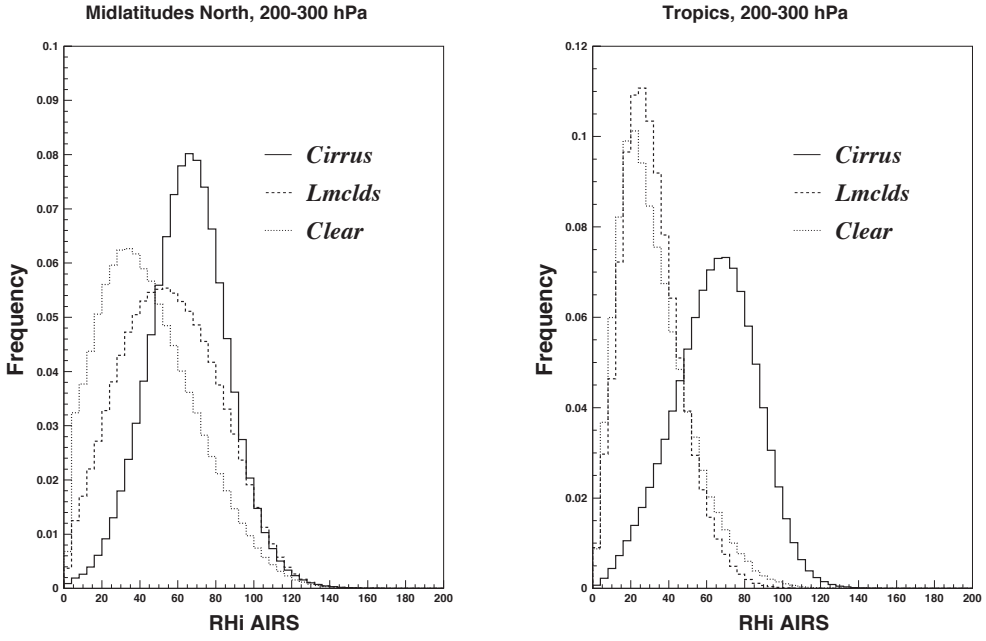

Fig. 3. Distributions of AIRS relative humidity RHi_A for three classes of AIRS cloud properties in two latitude bands: Northern Hemisphere midlatitudes (40–60°, left) and tropics (20° N–20° S, right). For lmclds and clear situations RHi_A is all measurements in pressure layers 200–250 and 250–300 hPa. For cirrus situations RHi_A is restricted to one of these two pressure layers enclosing the cloud pressure p_{cld}.

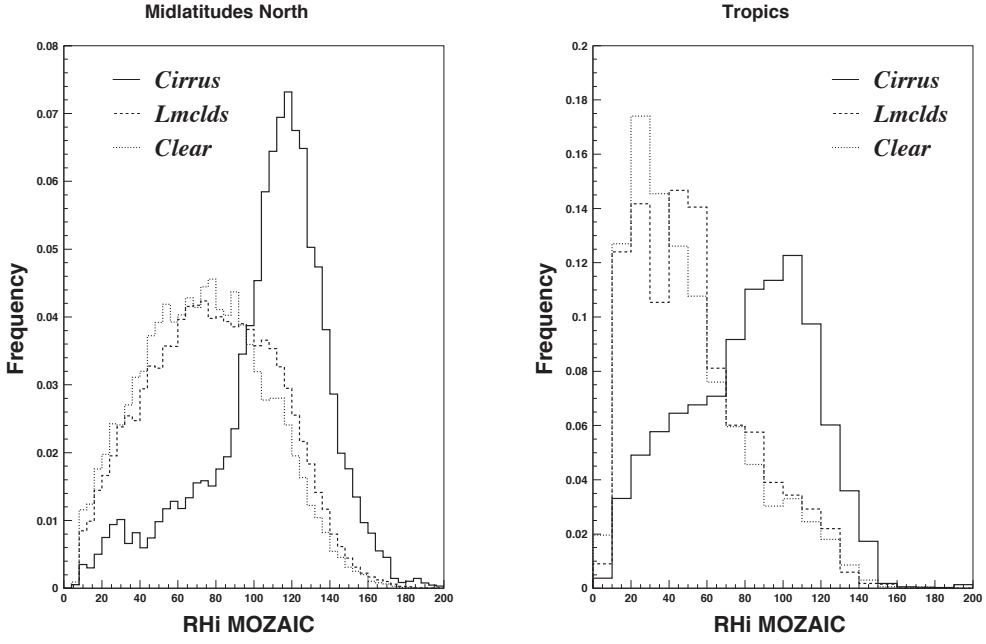

Fig. 4. Distributions of relative humidity seen by MOZAIC RHi_M for three classes of AIRS cloud properties in two latitude bands: Northern Hemisphere midlatitudes (40–60°, left) and tropics (20° N–20° S, right). For lmclds and clear situations RHi_M is all measurements between 200 and 300 hPa, for cirrus situations measurements are taken at pressures close to the cloud pressure so that $|p_M - p_{cld}| < 50$ hPa. The binning for the tropics is less resolved due to the smaller sample size in the tropics.

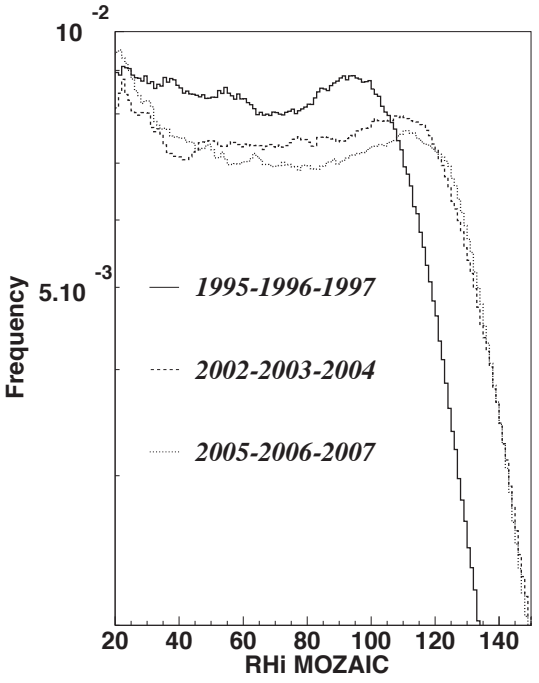

Fig. 5. Distributions of relative humidity seen by MOZAIC RHi_M for the years 1995-1996-1997 compared to distributions for 2002-2003-2004 and 2005-2006-2007.

for further overpasses of a region, which is very sparse for accurate statistics. 352 grid boxes have an average time step smaller than 10 days but 273 grid boxes have an average time step larger than 10 days, 67 grid boxes attain average delays larger than 100 days.

We derive relative humidity with respect to ice (from now onwards termed "RHi_M") as in Gierens et al. (1999) and only keep data of highest quality (tag "1") with $p_M < 500$ hPa and $T < 243$ K to avoid mixed-phase relative humidities (e.g. Pruppacher, 1994). Moreover, the same procedure as in Gierens et al. (1999) is applied to find out if measurements were taken in the lower stratosphere or in the upper troposphere. An ozone mixing ratio m_{O_3} of 130 ppbv is used as a threshold separating troposphere (lower values) and stratosphere (higher values). We have collocated these data with the AIRS data to (1) investigate relationships between MOZAIC relative humidity and AIRS cloud properties and (2) to develop a calibration method for the detection of ice supersaturation within the AIRS data.

2.4 AIRS-MOZAIC collocations and statistics

AIRS cloud properties are retrieved within each AIRS footprint of 13.5 km whereas RHi_A is computed within the AMSU footprint of about 40 km. Therefore, we use two different collocation schemes:

– when combining the AIRS cloud properties with MOZAIC relative humidity measurements we only keep the one flight measurement which is closest to the center of the AIRS footprint and which is inside the AIRS footprint.

– when combining AIRS RHi_A with MOZAIC RHi_M we first collect all MOZAIC single measurements located within the AMSU footprint and then choose the highest relative humidity RHi_M among the collection of collocated measurements. The maximum is chosen to increase the chances to detect ice supersaturation.

In both cases data have to be coincident within a timeframe of 30 min. A maximum of about 50 collocated MOZAIC measurements (from one flight) can reside within one AMSU footprint. The high coverage and the large amount of AIRS data between 2003 and 2007 lead to a relatively large set of statistics. Table 3 presents statistics of collocations for different AIRS cloudiness scenes in the upper troposphere ($p < 500$ hPa), separately for the Northern Hemisphere (NH) midlatitudes, tropics and all statistics. AIRS cloudiness scenes are divided into clear sky ("clear"), low and mid-level clouds ("lmclds", $p_{cld} > 440$ hPa) and high clouds ("cirrus", $p_{cld} < 440$ hPa). In brackets we indicate the fraction of these scenes with respect to all MOZAIC-AIRS collocations (per latitude band and total). Statistics are higher in the NH midlatitudes linked to the density of commercial flights.

3 Synergy of AIRS and MOZAIC

3.1 AIRS and MOZAIC relative humidities in dependence of cloudiness

Since the humidity retrieved by AIRS corresponds to a value integrated over a vertically extended atmospheric layer, the average RHi_A is smaller than the maximum RHi within this layer. In addition, AIRS measurements used for the retrieval of atmospheric profiles have been "cloud cleared" (see Sect. 2.1). As a consequence RHi_A distributions appear drier in the presence of cirrus clouds than expected from in situ measurements.

The collocation of AIRS and MOZAIC allows us to evaluate RHi for different cloudiness situations from AIRS. Therefore, we use the AIRS scene identification of Sect. 2.2 and compare RHi distributions between 200 and 300 hPa (RHi_A of the 200–250 and 250–300 hPa layers) from AIRS and from MOZAIC (RHi_M) for three cloudiness situations: cirrus, clear sky and low/mid-level clouds), separately in the NH midlatitudes and the tropics. We only consider data below the tropopause. This is ensured by the MOZAIC criterion $m_{O_3} < 130$ ppbv and by the tropopause altitude provided in the AIRS L2 data. Figure 3 illustrates the dry bias in the RHi_A distributions for the three cloudiness situations. Even if there is a clear distinction between cirrus and clear sky in the upper troposphere, the peaks of the RHi_A distributions for cirrus lie in both regions at about 70 %, as has already been

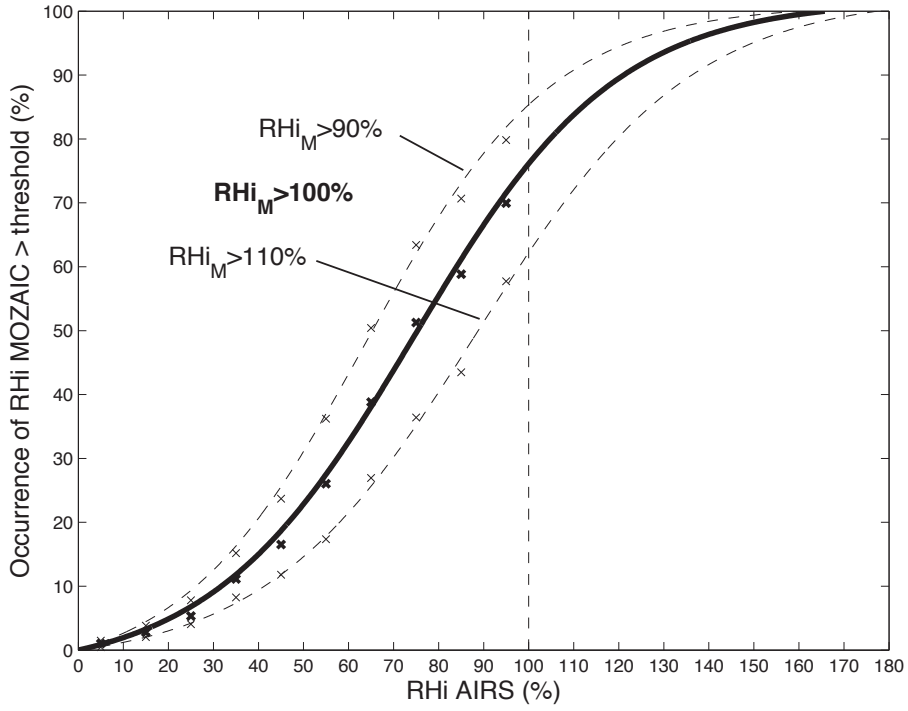

Fig. 6. Occurrence probability of ice supersaturation seen from MOZAIC as a function of AIRS relative humidity. MOZAIC supersaturation is declared when $RHi_M > 90\,\%$, $RHi_M > 100\,\%$, or $RHi_M > 110\,\%$.

stated for TOVS (Stubenrauch and Schumann, 2005) and in contrast to 100 % what would have been expected from in situ measurements (Ovarlez et al., 2002; Immler et al., 2008). It is interesting to note that in the tropics the peaks of clear sky and of clear sky in the upper troposphere (lmclds) coincide at around 20 %, the peak of the lmclds distribution in the NH midlatitudes lies between the one of clear sky and lmclds. This could be explained by more midlevel clouds in the NH midlatitudes than in the tropics, especially linked to winter storm tracks (Stubenrauch et al., 2010), and since RHi is integrated over a whole layer and the cloud pressure retrieved by AIRS corresponds approximately to the middle of the cloud it could be possible that in some cases part of the cloud is included in the layer.

Figure 4 presents RHi_M distributions from MOZAIC, separately for the same three AIRS scene types. For situations involving cirrus clouds we observe a peak frequency at 115–120 % for the NH midlatitudes and around 100 % for the tropics. The distributions for clear sky and lmclds peak in both regions lower, again with lower peak values in the tropics. We have to explain two issues: first why we find differences between NH midlatitudes and tropics for the cirrus distributions and second why the peak in the NH midlatitudes lies higher than expected.

In the tropics, the cruise altitude of aircraft does not coincide with the altitude where cirrus clouds are most commonly found (100–150 hPa in Lamquin et al., 2008). Therefore it is likely that the relatively drier values and a larger standard deviation in this region are induced by the presence of dissipating cirrus and, possibly, shallower ice supersaturated layers, or that the flight altitude is simply not coincident with the cirrus layer.

The peak value at RHi_M larger than 100 % could indicate that most of the measurements are made in the vicinity of cirrus where there is potentially higher ice supersaturation. However, our observation of a peak higher than saturation agrees with the distributions of RHi_M (measured in 2003) in Gettelman et al. (2006a) where RHi_M decreases more sharply after 120 % but disagrees with distributions from Gierens et al. (1999) obtained from earlier MOZAIC data (1995–1997). Indeed, Gierens et al. (1999) show probability distributions of either tropospheric or stratospheric RHi_M. These distributions show a decrease beyond 100 % with a concomitant bulge highlighting the statistics of measurements inside cirrus clouds (Spichtinger et al., 2004).

To understand these differences, Fig. 5 shows distributions of tropospheric RHi_M ($p < 500$ hPa, $T < 243$ K and $m_{O_3} < 130$ ppbv) obtained from MOZAIC by comparing three time intervals: 1995 to 1997, 2002 to 2004 and 2005 to 2007. Compared to the years 1995 to 1997 the distributions over the periods 2002–2004 and 2005–2007 show a significant shift of about 10 %, likely due to a calibration problem (H. Smit, personal communication, 2010).

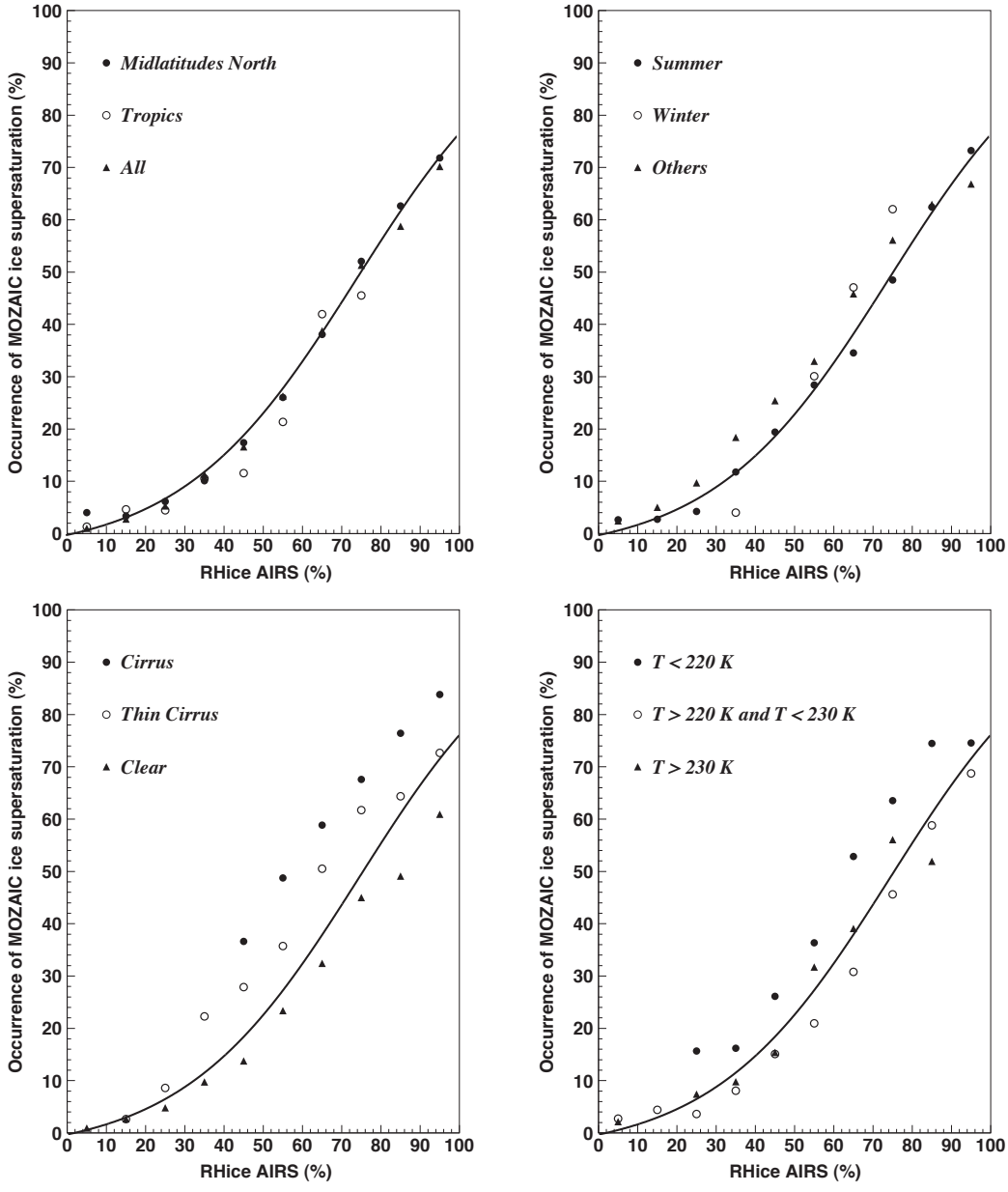

Fig. 7. Occurrence probability of ice supersaturation seen from MOZAIC as a function of AIRS relative humidity. MOZAIC supersaturation is declared when $RHi_M > 100\,\%$. Top left: sorted by regions, top right: sorted by seasons for the northern hemisphere midlatitudes. Bottom left: sorted by cloud types, bottom right: sorted by temperature. In all figures the baseline S-function ($RHi_M > 100\,\%$) from Fig. 6 is reproduced in plain line.

In the following we consider the occurrence of ice supersaturation detected by MOZAIC. For this purpose we need to empirically calibrate the data (for the MOZAIC time period used here: 2002–2007) by shifting the detection threshold by 10 %: MOZAIC detects ice supersaturation only when $RHi_M > 110\,\%$. This is all the more reliable since the shape of the decreasing slope after saturation is unchanged. Also, as Gierens et al. (1999) suggest for values of RHi_M around saturation, an uncertainty $\Delta RHi_M = \pm 10\,\%$ is taken into account.

3.2 Impact of fixed flight altitudes

We have to keep in mind that MOZAIC measurements are taken at only one level, corresponding to the actual flight altitude. There is no information on the thickness of supersaturated layers. Even if the MOZAIC measurement is below an assumed ISS threshold of 110 %, there may exist a layer of ISS below or above flight altitude. This potentially underestimates the occurrence of ice supersaturation detected by MOZAIC within the AIRS pressure layers of about 2 km.

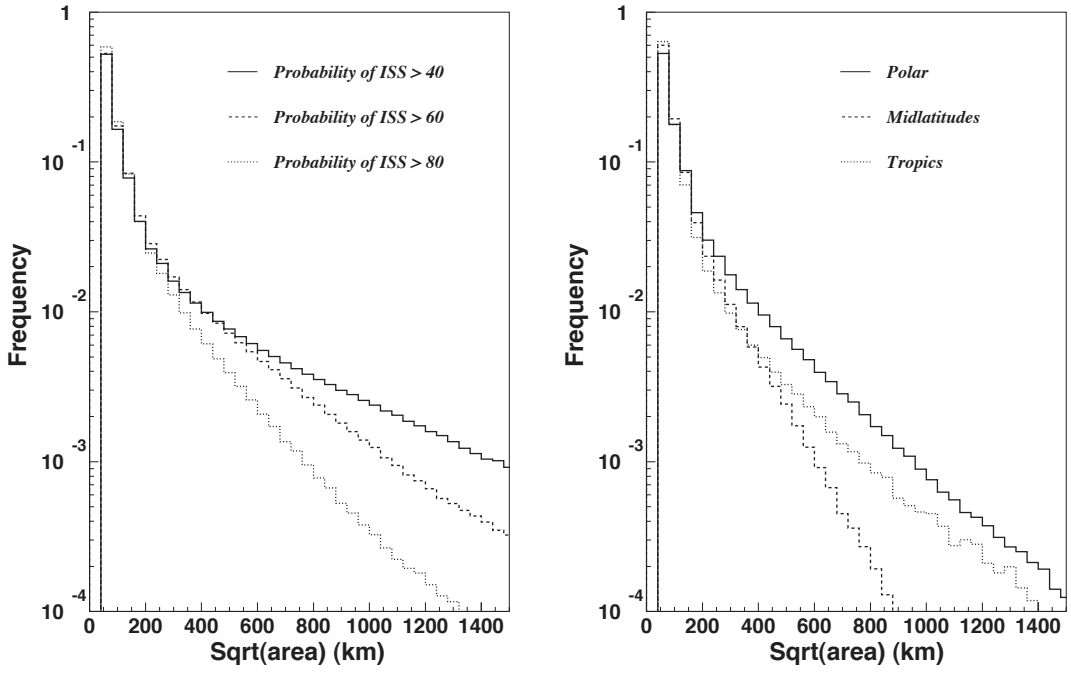

Fig. 8. Characteristic size of clusters of ice supersaturated areas from AIRS. Left: $S > 40\,\%$, $S > 60\,\%$ or $S > 80\,\%$, all regions combined. Right: $S > 80\,\%$ for polar regions (latitude higher than 70° N or S), midlatitudes (40–60° N and S) and tropics (20° N–20° S).

To compensate for this effect we must lower the relative humidity threshold for ice supersaturation detection in MOZAIC. However, lowering this threshold increases the probability of false-alarms, that is to say the amount of supersaturation detected when there is no supersaturation in reality.

For the determination of a reasonable threshold we apply the Peirce skill-score method (Peirce, 1884) to simulate the success of ice supersaturation detection. It has notably been used (and widely explained) in Rädel and Shine (2007) for an evaluation of the ability of radiosounding measurements to detect cold ice supersaturated regions nesting persistent contrails. We also need a dataset of RHice profiles which is given by a collection of radiosoundings from routine measurements at Lindenberg, Germany. These radiosounding measurements are corrected in the upper troposphere (Leiterer et al., 2005) and detect ice supersaturation (Spichtinger et al., 2003a; Lamquin et al., 2009). We only consider profiles up to 200 hPa because of the the tropopause in Lindenberg.

For each AIRS pressure layer a Monte-Carlo simulation is made over the collection of radiosonde profiles: for each profile altitudes with their corresponding measurements of relative humidity are randomly chosen inside the pressure layer. The success to detect ice supersaturation is evaluated by varying the threshold between 0 and 100 % using the Peirce skill-score. For the pressure layers 200–250 and 250–300 hPa the score is maximum for a relative humidity threshold of about 90 %. The distributions for the pressure layers 300–400 and 400–500 hPa are slightly broader with a peak around 85 %. The difference is linked to the slightly larger vertical extension of these layers.

In the AIRS-MOZAIC collocations most of the statistics arise from flight altitudes between 200 and 300 hPa, therefore the skill-scores obtained for the pressure layers 200–250 and 250–300 hPa must preferably be taken into account. As a consequence, a decrease of 10 % is applied to the MOZAIC relative humidity threshold for the detection of ice supersaturation within the boundaries of the AIRS pressure layers.

To conclude, we consider ISS to be detected by MOZAIC at some location of a pressure layer when $\mathrm{RHi_M} > 100 \pm 10\,\%$. Although this threshold would have naturally been used, only an understanding of the relationships presented above leads to its correct interpretation.

3.3 A calibration method for the determination of ice supersaturation occurrence within AIRS pressure layers

The principle of the method was introduced in Lamquin et al. (2009). It is based on the determination of an occurrence probability of ISS as a function of coarse relative humidity measurements integrated over pressure layers. This occurrence probability can either be the probability of "at least once" supersaturation (supersaturation exists

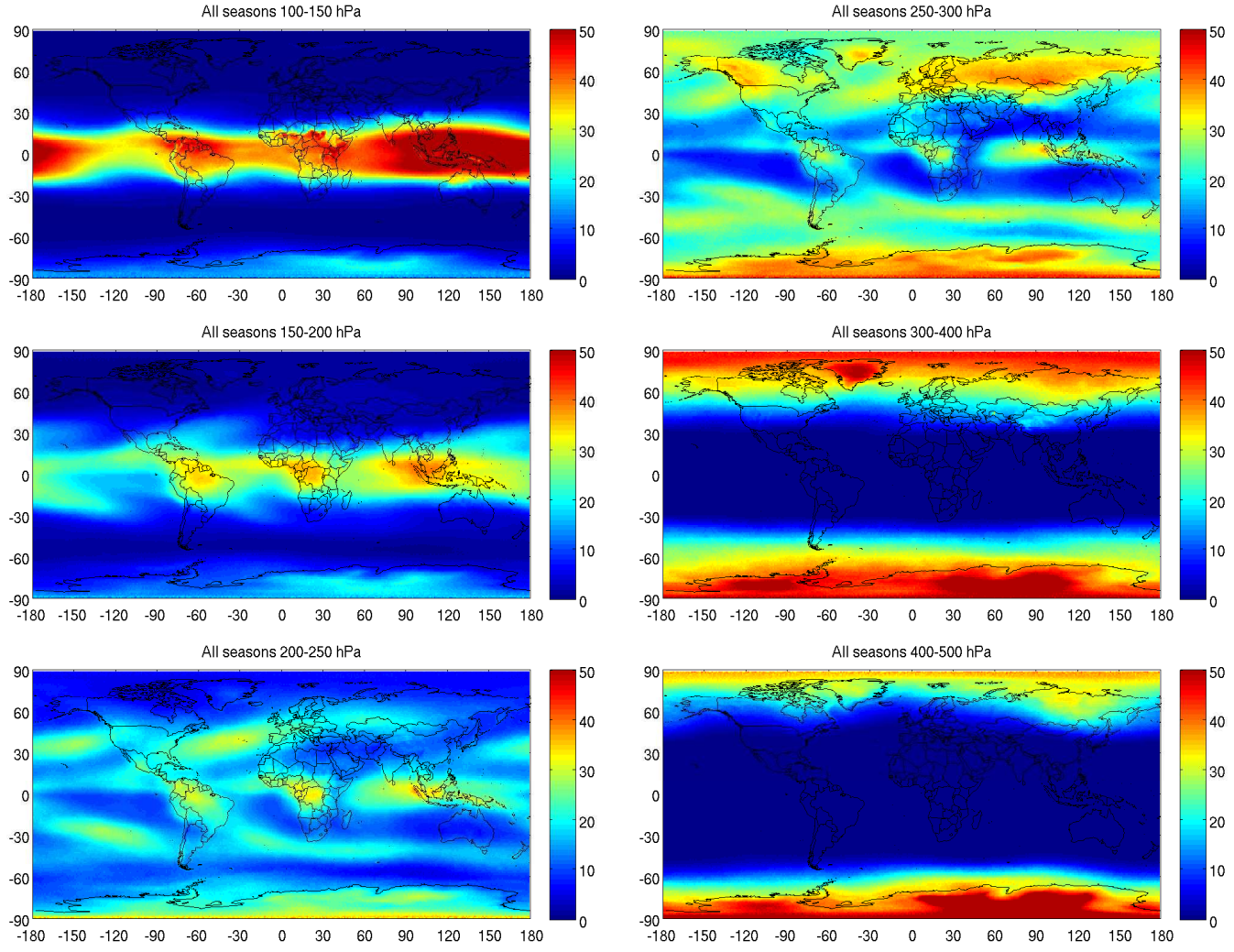

Fig. 9. Ice supersaturation occurrence frequencies (%) from AIRS in the pressure layers 100–150, 150–200, 200–250, 250–300, 300–400 and 400–500 hPa. Only good quality data used. 7-yr statistics 2003–2009.

Table 4. Parameters a and b of the Weibull distributions fitted from the histograms of Fig. 8 and their correlation coefficient.

Case (percent above 40, 60, 80)	a	b	correlation coefficient
$S(\mathrm{RHi_A}) > 40$, global	0.099	0.516	0.988
$S(\mathrm{RHi_A}) > 60$, global	0.067	0.613	0.994
$S(\mathrm{RHi_A}) > 80$, global	0.064	0.664	0.993
$S(\mathrm{RHi_A}) > 80$, polar	0.028	0.804	0.994
$S(\mathrm{RHi_A}) > 80$, midlatitudes	0.034	0.807	0.994
$S(\mathrm{RHi_A}) > 80$, tropics	0.098	0.596	0.989

somewhere within the layer) or the probability of supersaturation weighted by the thickness of the supersaturated fraction of the layer (the weight being one if supersaturation covers the whole pressure layer). The first approach is equivalent to the second approach when using a weight of one, whether the supersaturated layer is thin or thick. According to Spichtinger et al. (2003a) and Rädel and Shine (2007) ice supersaturated layers are indeed on average thinner (about 500–700 m) than the vertical spacing of the AIRS pressure layers (about 2 km).

In Lamquin et al. (2009) the "at least once" approach was proposed because no accurate information on the thickness of supersaturated layers could be given. Dickson et al. (2010) investigated the weighted approach by using a very large set

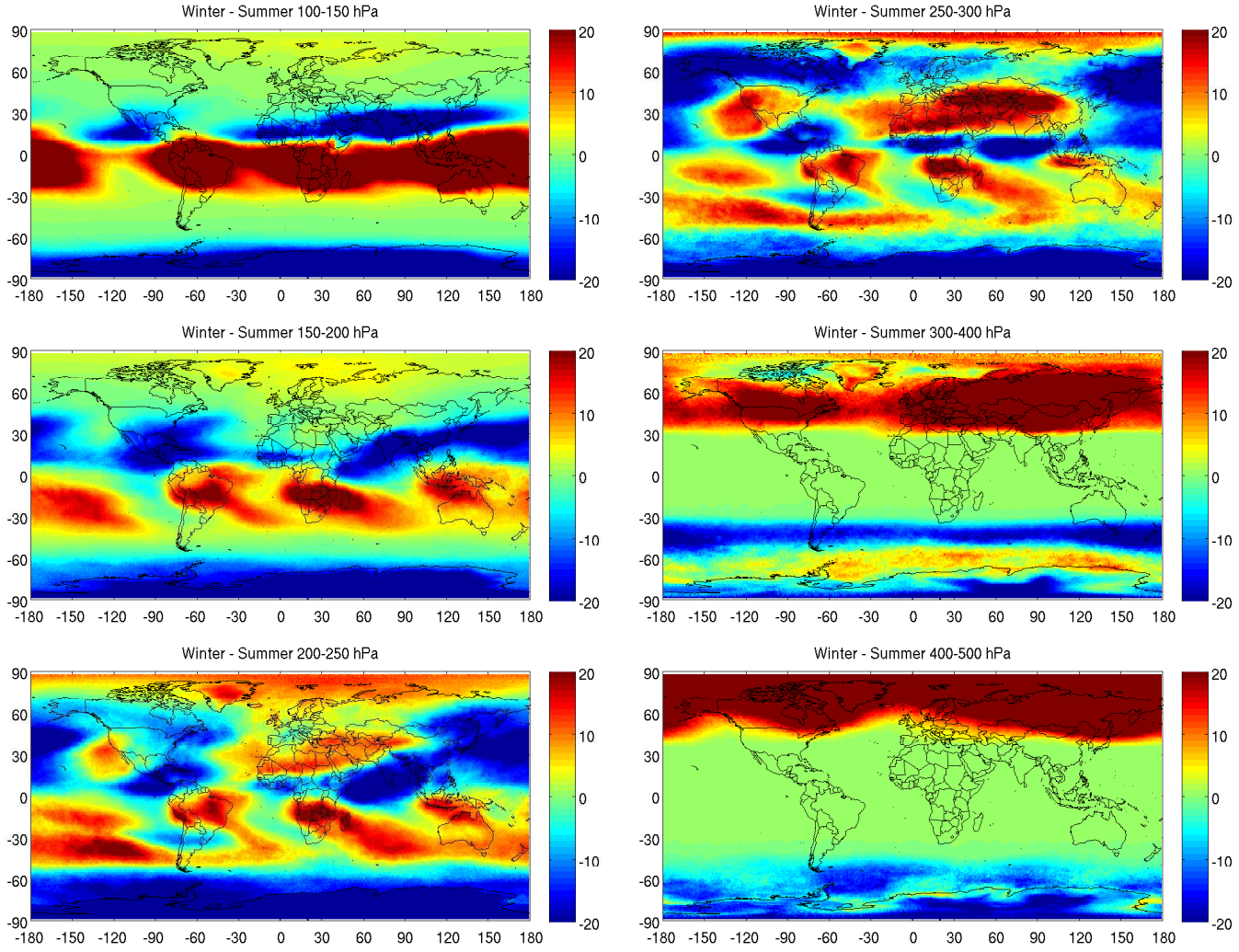

Fig. 10. Ice supersaturation occurrence frequencies (%) from AIRS in the pressure layers 100–150, 150–200, 200–250, 250–300, 300–400 and 400–500 hPa. Boreal winter – boreal summer. Only good quality data used. 7-yr statistics 2003–2009.

of radiosonde measurements, they show that the so-called "S-function" depends mostly on the vertical resolution of the coarsely-determined relative humidity.

As MOZAIC measurements do not allow the determination of the thickness of ice supersaturated layers, we must use the "at least once" approach and make a sensitivity analysis. The "at least once" statistics lead to higher ISS occurrences than the statistics weighted by the thickness of the supersaturated layers (Figs. 3 and 4 of Rädel and Shine, 2007). This is important to keep in mind when comparisons are presented in Sect. 5 as we will compute ISS occurrence frequencies in other datasets in a similar way over pressure layers of finite depth.

We now build the "S-function" by examining the probability of ice supersaturation computed from MOZAIC data collocated with AIRS relative humidity $\mathrm{RHi_A}$. Figure 6 then relates $\mathrm{RHi_A}$ and $\mathrm{S_{Th}(RHi_A)}$, the occurrence probability of ice supersaturation determined by the condition $\mathrm{RHi_M} > \mathrm{Th}\,\%$ with either $\mathrm{Th} = 90\,\%$, $\mathrm{Th} = 100\,\%$ or $\mathrm{Th} = 110\,\%$ to take into account the 10 % uncertainty of MOZAIC.

The statistics drop progressively as $\mathrm{RHi_A}$ increases, without enough statistics at $\mathrm{RHi_A} > 100\,\%$ (less than 100 events per interval). Only statistically significant pairs ($\mathrm{RHi_A}$, $\mathrm{S_{Th}(RHi_A)}$) are shown, and each curve is fitted for further use. Hyperbolic tangent functions are the most convenient to that end and the fits give

- $S_{90}(\mathrm{RHi_A}) = 48.21 + 52.77 \cdot \tanh((\mathrm{RHi_A} - 63.90)/41.26)$,
- $S_{100}(\mathrm{RHi_A}) = 49.04 + 52.74 \cdot \tanh((\mathrm{RHi_A} - 74.49)/44.94)$, and
- $S_{110}(\mathrm{RHi_A}) = 50.01 + 52.40 \cdot \tanh((\mathrm{RHi_A} - 88.78)/47.26)$.

Two conclusions can be drawn: first, we see that, even for $\mathrm{Th} = 110\,\%$, a significant probability of ice supersaturation is

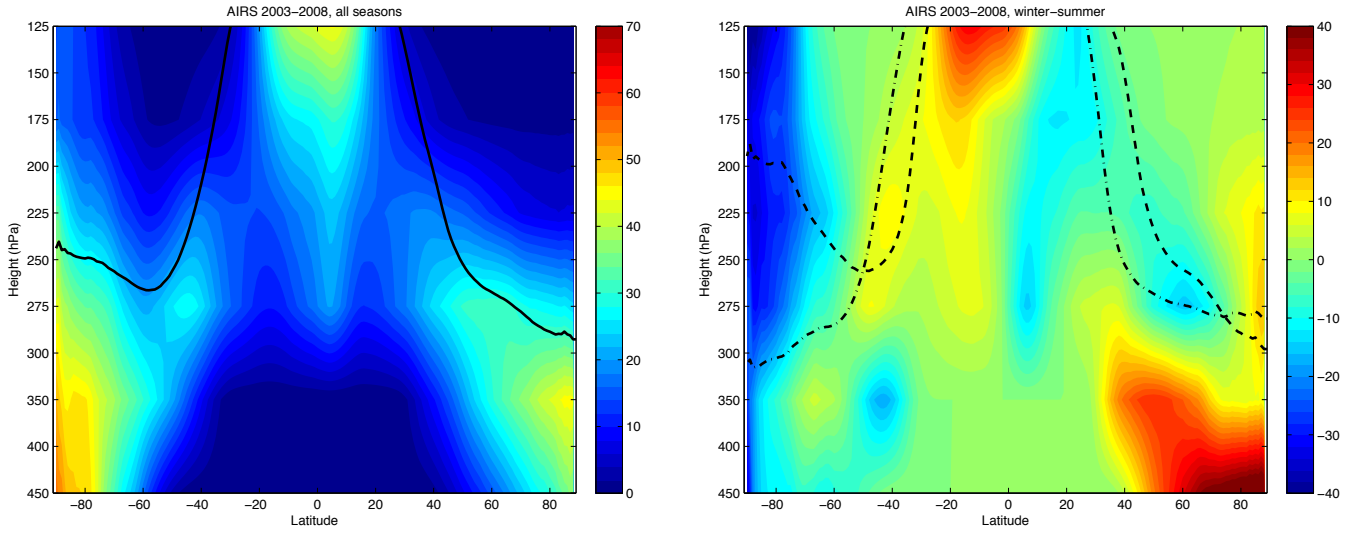

Fig. 11. Zonal means of ice supersaturation occurrence frequencies (%) from AIRS using $S_{100}(\mathrm{RHi_A})$ (left) along with boreal winter minus boreal summer differences (right). Plain line: zonal-mean tropopause (all seasons). Dashed line: zonal mean summer tropopause. Pointed dashed line: zonal mean winter tropopause. Only good quality data used. 7-yr statistics 2003–2009.

found when $\mathrm{RHi_A}$ is smaller than 100 %. This is what we expected, as Kahn et al. (2008) and Lamquin et al. (2008) have already shown that very shallow ice clouds are concomitant with low $\mathrm{RHi_A}$, highlighting the impact of the coarse vertical resolution of the sounder.

Second, the occurrence of ice supersaturation reaches only about 85 % for $\mathrm{RHi_A}$ values around saturation even for Th = 90 %. It can be argued that MOZAIC does not always locate ISS lying within the pressure layer even though we statistically compensate the effect of having fixed flight altitudes in the timeframe of the collocation. However, when $\mathrm{RHi_A} \approx 100$ % a substantial part of the pressure layer must be very humid thus decreasing the probability that MOZAIC misses ISS. Another explanation considers non-linear effects of the AIRS vertical resolution on $\mathrm{RHi_A}$: saturation does not mean that the whole profile inside the layer is saturated. Unfortunately it is not possible to investigate this further as we do not have information on relative humidity profiles with MOZAIC.

To explore the stability of the S-function Fig. 7 distinguishes latitude bands (top left), seasons in the NH mid-latitudes (top right), cloud scenes as inferred from the nine AIRS footprints within each AMSU footprint (bottom left) and temperature intervals given by the MOZAIC measurements (bottom right). Only $\mathrm{RHi_A}$ values lower than saturation are shown because higher values do not provide enough statistics. In Fig. 7 occurrence probabilities of ice supersaturation are determined with Th = 100 %. The regional and seasonal variabilities are rather small compared to variabilities obtained for different temperature ranges or cloud scenes.

The interpretation of the differences observed for different cloud scenes is quite straightforward. We distinguish between clear and cloudy situations in the upper troposphere: "clear" meaning "no clouds in the upper troposphere", that is to say either clear sky or low and mid-level clouds. Using the retrieved emissivity we further separate cirrus situations into "thin cirrus" ($\epsilon_{\mathrm{cld}} < 0.5$) and "cirrus" ($\epsilon_{\mathrm{cld}} > 0.5$). Clearly, the occurrence probability of ice supersaturation $S(\mathrm{RHi_A})$ is increasing with cloudiness in the upper troposphere. This highlights the effect of fixed flight altitudes of MOZAIC within the AIRS pressure layers. With increasing cloudiness portions of the atmospheric profiles with high relative humidity are extending vertically, thus increasing the probability for MOZAIC aircraft to fly through supersaturated areas (either inside or in the vicinity of clouds). On average, the impact of fixed flight altitudes has been taken into account by lowering the MOZAIC detection threshold Th. It could be considered relevant to use different S-functions depending on the cloud scene but we are interested in the occurrence of ice supersaturation within a pressure layer, independently of its vertical extent. The differences in Fig. 7 for different cloud scenes should not be considered as a bias in the present analysis.

For different temperature ranges there is no clear distinction between results obtained for the temperature ranges $220 < T < 230$ K and $T > 230$ K (with still $T < 243$ K). However, Fig. 7 exhibits higher occurrence probability of ice supersaturation for the coldest temperatures ($T < 220$ K). Gierens et al. (1999) show that ice supersaturated regions are, on average, colder than other regions in the upper troposphere. By selecting the coldest temperatures we might in turn get higher ice supersaturation occurrence probability

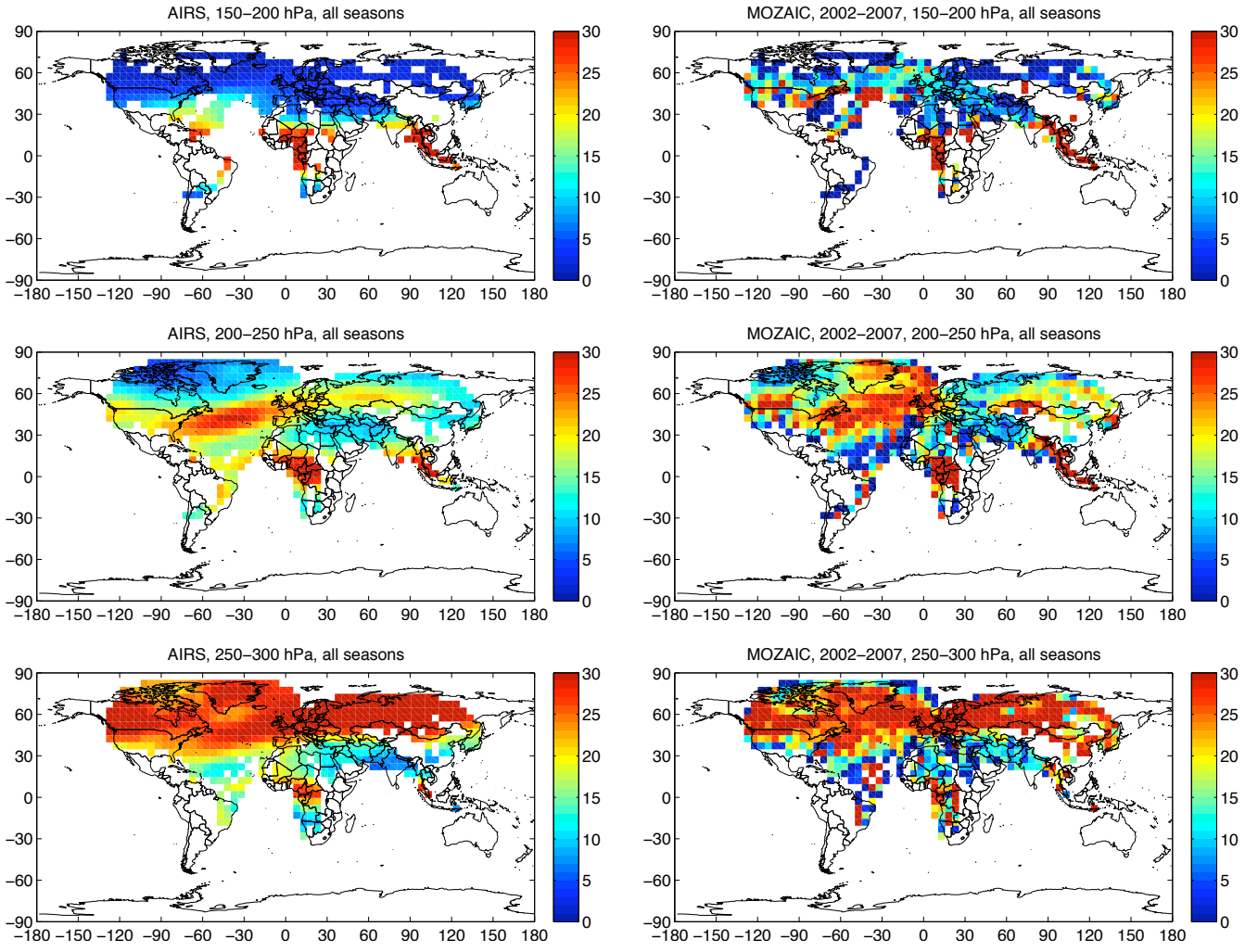

Fig. 12. Ice supersaturation occurrence frequencies (%) from AIRS (left) and MOZAIC (right) in the pressure layers 150–200, 200–250 and 250–300 hPa.

simply by having a greater chance that MOZAIC meets supersaturation. Possible non-linear effects of the AIRS vertical resolution on $\mathrm{RHi_A}$ might influence this comparison as temperature can vary as much as 5 to 10 K between the edges of the pressure layers and MOZAIC can fly anywhere inside the layer. We can therefore only relate the observed differences to global uncertainties. Again, we cannot investigate this any further as MOZAIC does not provide information on the vertical distribution of temperature and humidity.

Overall the S-function appears quite stable with differences remaining within the uncertainties arising from MOZAIC and its coupling with AIRS. The global uncertainty on this method is set by the two bracketing S-functions $S_{90}(\mathrm{RHi_A})$ and $S_{110}(\mathrm{RHi_A})$.

4 Ice supersaturation from AIRS and comparisons with MOZAIC and CALIOP

4.1 Horizontal extent of ice supersaturated areas

The horizontal extent of ice supersaturated layers is a key feature for a large-scale model's parameterization of ice supersaturation. Ice supersaturation can be detected from each AIRS observation only in a probabilistic way. In fact the S-function only gives the probability $S(\mathrm{RHi_A})$ that an observation contains ice supersaturation. To evaluate the horizontal extent of ice supersaturated areas, we link neighbouring observations satisfying the same condition on this probability: $S(\mathrm{RHi_A}) > \alpha$. To do so we built a simple clustering algorithm which groups AIRS observations belonging to the same orbits and satisfying such condition. We use either $\alpha = 40\,\%$, $\alpha = 60\,\%$, or $\alpha = 80\,\%$. Each observation is assigned the size of a square, the side of which is the diameter of the AMSU footprint and we take into account the

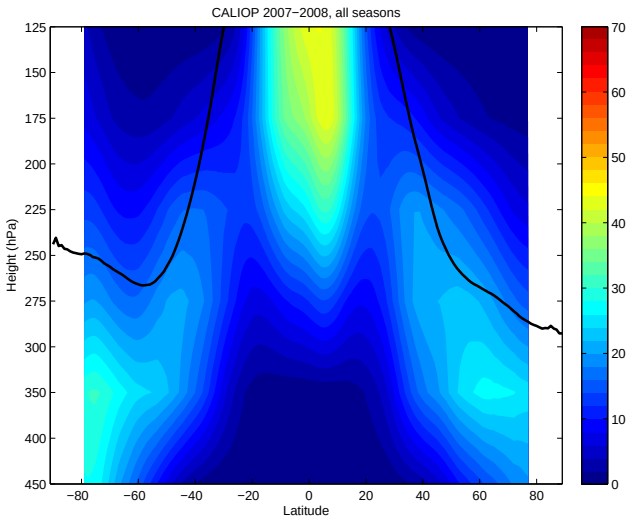

Fig. 13. Zonal means of high cloud occurrence from CALIOP for the years 2007–2008. Plain line: zonal-mean tropopause (all seasons).

variability of this size with the angle of observation. Clusters are constructed by grouping neighbouring observations of the same orbits and we do not relate adjacent orbits, therefore the clusters are limited by the size of the AIRS swath (1650 km). The results possibly underestimate the true size of the clusters but the figures suggest that only very few clusters are extremely large.

Figure 8 shows the distributions of the characteristic size (square root of the total area) of the clusters for (left) the three values of α for all regions combined and for (right) $\alpha = 80\,\%$ for three latitude bands: polar, ($> 70°$), midlatitudes (40–60° N and S) and tropics (20° N–20° S). When α is smaller the condition $S(\mathrm{RHi_A}) > \alpha$ is less restrictive and therefore the cluster sizes get larger. At fixed $\alpha = 80\,\%$ the cluster sizes are larger in the polar regions and in the tropics, concomitant with higher ISS occurrence frequencies, than in the midlatitudes (see below Fig. 9). Overall, the large majority of characteristic sizes are smaller than 200 km which agrees qualitatively with Gierens and Spichtinger (2000).

These distributions can be fitted by Weibull distributions (Gierens and Brinkop, 2002), i.e. functions of the form $abx^{b-1}e^{-ax^b}$. Using their cumulative distribution $F(x) = 1 - e^{-ax^b}$ a linear relationship exists between $\mathrm{loglog}1/(1-F)$ and $\log(x)$ as $\mathrm{loglog}1/(1-F) = \log(a) + \mathrm{loglog}(e) + b\log(x)$ (log is here with base 10). The histograms in Fig. 8 are then easily fitted using this relationship and Table 4 shows the parameters a and b of the Weibull function associated with each of these histograms as well as the very good correlation coefficient between the fit and the original histogram.

4.2 Climatology of ice supersaturation from AIRS

We have built a climatology of ice supersaturation occurrence by using $S_{100}(\mathrm{RHi_A})$ as a weighting function over each value $\mathrm{RHi_A}$ determined from the AIRS observations. The uncertainties are estimated by using $S_{90}(\mathrm{RHi_A})$ and $S_{110}(\mathrm{RHi_A})$. To avoid potential mixed-phase situations we include a temperature condition $\mathcal{T}$ which is either 0 or 1. $\mathcal{T}$ is set to zero when the temperature at the bottom of the pressure layer is higher than 243 K.

ISS occurrence frequencies are computed at a spatial resolution of 1° lat × 1° lon for each pressure layer p as

$$\mathrm{ISS}_p = \frac{\sum_{i=1}^{N} S_{100}(\mathrm{RHi_A}) \cdot \mathcal{T}}{N} \quad (1)$$

where N is the number of profiles of good quality in the upper troposphere over $1 \times 1°$.

Figure 9 presents geographical maps of ice supersaturation occurrence in the upper troposphere for six AIRS pressure layers between 100 and 500 hPa. Statistics are averaged over the period 2003 to 2009 including daytime and nighttime observations. We recall that results for pressure layers 100–150 and 150–200 hPa are subject to larger uncertainties because of the AIRS lower reliability at such high altitudes.

Whereas the function $S(\mathrm{RHi_A})$ is obtained from tropospheric data only, it is also used when the pressure layer is partly or entirely within the stratosphere. In these cases $\mathrm{RHi_A}$ is an "average" between the moister part of the layer lying in the troposphere and the drier part lying in the stratosphere. $\mathrm{RHi_A}$ is decreased compared to its tropospheric counterpart. However, $S(\mathrm{RHi_A})$ is also decreased which represents the fact that ice supersaturation occurrence probability within the entire pressure layer is decreased. We assume that the S-function $S(\mathrm{RHi_A})$ smoothly captures the transition from tropospheric to stratospheric air and ISS_p decreases accordingly as we progress upward.

In Fig. 9 ice supersaturation occurrence frequencies mainly follow the tropopause with high frequencies close to the tropical tropopause in the pressure layer 100–150 hPa, local maxima in connection with the storm tracks and jet streams in the midlatitudes at 200–250 hPa, and then close to the Arctic tropopause (about 300 hPa). Although caution is raised at such altitudes, the tropical maximum at 100–150 hPa agrees qualitatively with clear-sky ISS statistics from the Microwave Limb Sounder (MLS) in Spichtinger et al. (2003b) at 147 hPa with frequencies up to 50 % over areas of deep convection. The seasonal difference between winter and summer is presented in Fig. 10. It shows higher supersaturation frequencies during boreal winter, which again agrees with Spichtinger et al. (2003b).

In the polar regions Treffeisen et al. (2007) show occurrence frequencies of ISS from 15 yr of corrected radiosonde measurements over Ny-Ålesund, Svalbard. They show a strong seasonal cycle of ISS frequencies with a maximum

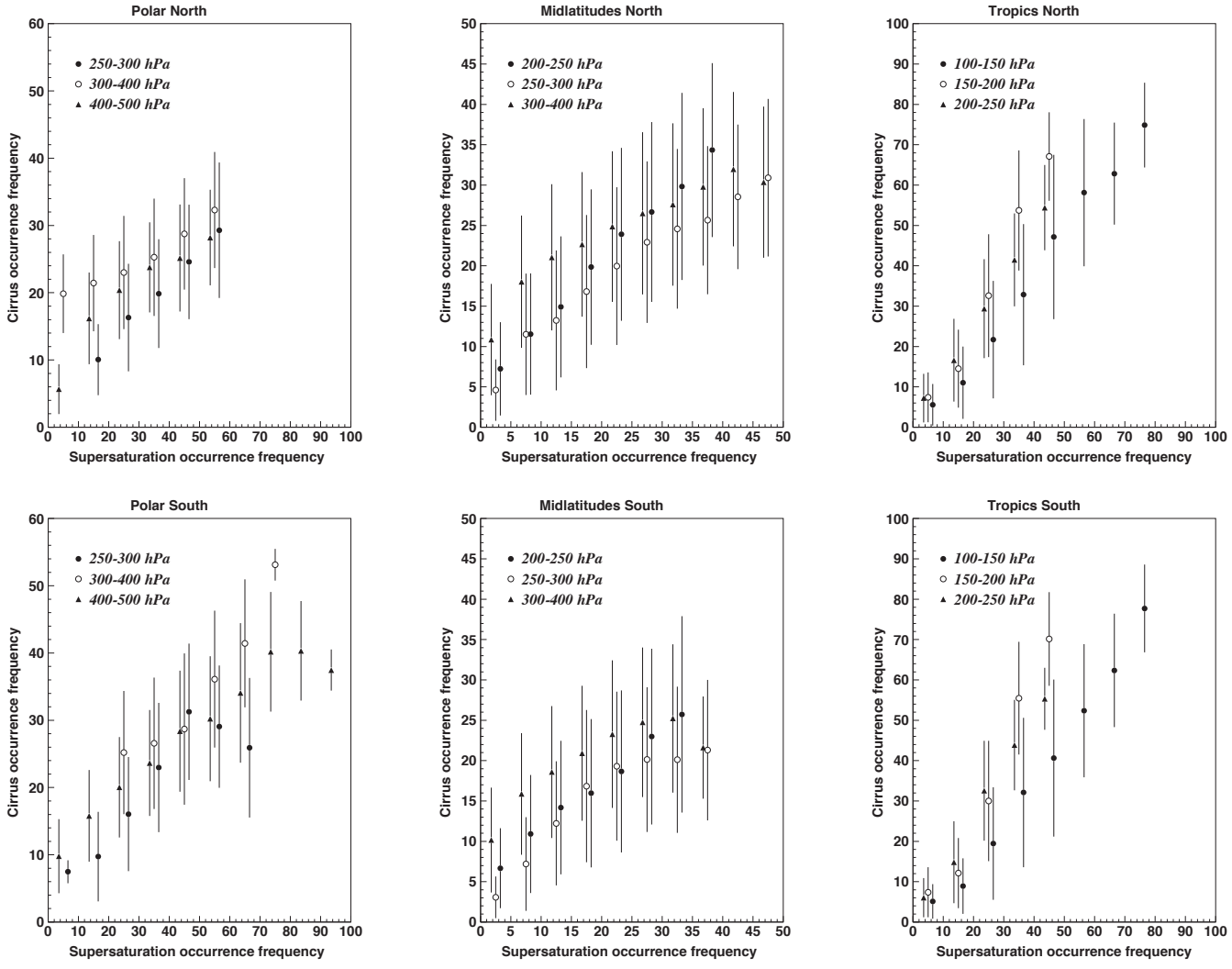

Fig. 14. Relationships between cirus cloud occurrence frequencies (%) determined from CALIOP and ice supersaturation occurrence frequencies (%) from AIRS. Polar regions (60–90° N and S separately), midlatitudes (30–60° N and S separately), and tropics (0–30° N and S separately).

during boreal winter (about 35 % in some portions of the atmosphere in their Fig. 6), in agreement with our results.

If instead of determining an ISS occurrence probability from RHi_A by using the S-function inferred from MOZAIC one computes ISS occurrence frequencies just by applying a threshold of 100 % on RHi_A, then the results would be close to the ones of Gettelman et al. (2006a). The fundamental difference between both methods lies in the determination of the occurrence of ISS independent of the thickness of the ISS layer in our method and of ISS over vertically very extended atmospheric layers in Gettelman et al. (2006a). Therefore, our ISS occurrence frequencies have overall larger values and seasonal amplitudes than the ones in Gettelman et al. (2006a).

Figure 11 shows the zonal means of ISS occurrences for all seasons combined (left) along with the differences between boreal winter and summer (right). The corresponding zonal mean tropopause is computed from the AIRS data. The electronic supplement includes the zonal means of ISS occurrences for winter (black lines) and for summer (red lines). Uncertainties are indicated in dashed by using $S_{90}(RHi_A)$ and $S_{110}(RHi_A)$. The relative uncertainty is about ± 20 %. The highest ISS occurrence frequencies are found close to the tropopause in the tropics and in the polar regions with maxima of about 50 %.

4.3 Comparison with MOZAIC ISS statistics

Although the climatology from MOZAIC is not global, an evaluation of the AIRS climatology can be made over areas covered by the MOZAIC flight paths (NH midlatitudes mainly). We restrict the analysis to the period 2002–2007 common to both datasets.

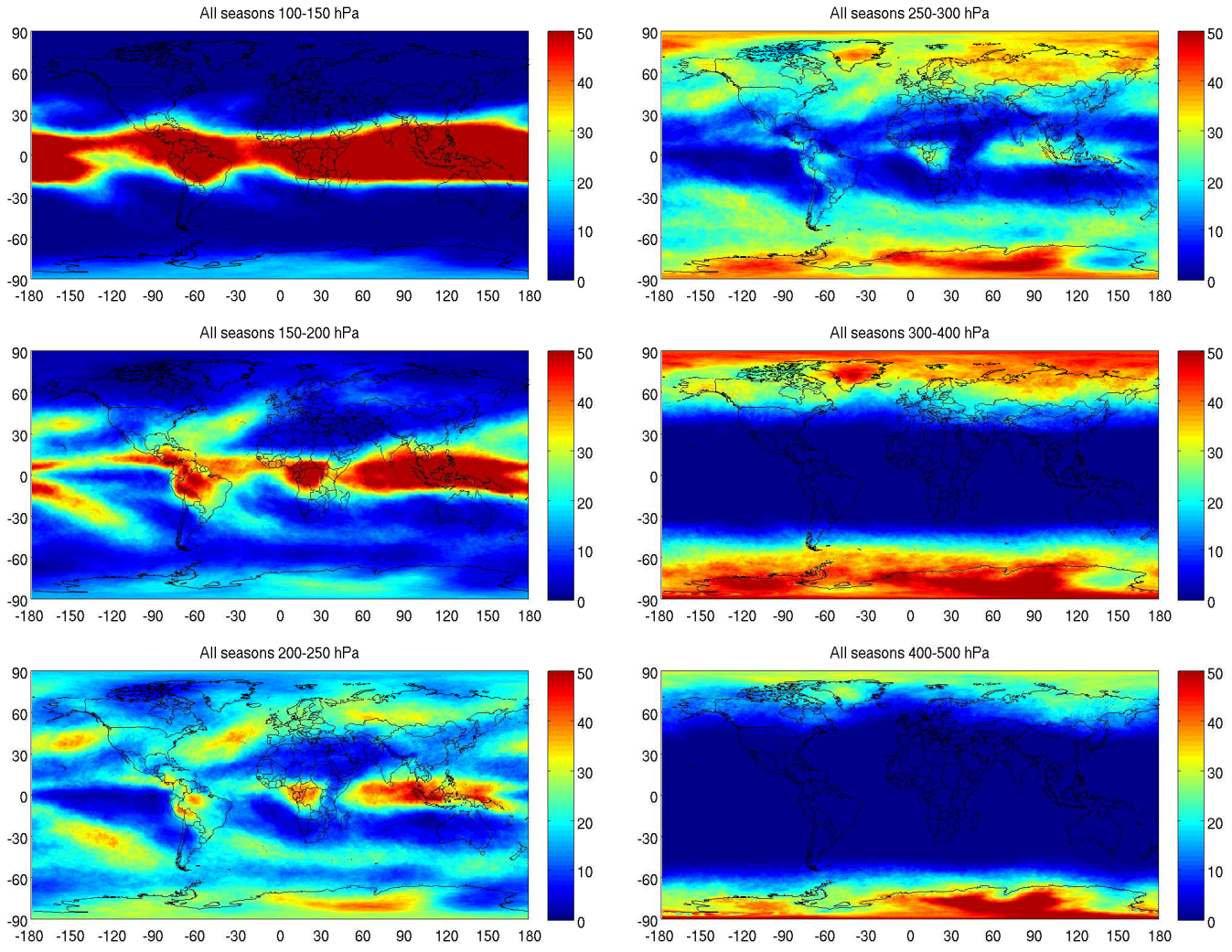

Fig. 15. Ice supersaturation occurrence frequencies (%) from ECMWF ("layer supersaturation" scheme) in the pressure layers 100–150, 150–200, 200–250, 250–300, 300–400 and 400–500 hPa. Year 2007.

To compute ISS occurrence with MOZAIC we follow Gierens et al. (2000) and collect MOZAIC data over 5° lat × 5° lon grid cells, separately in the three pressure layers 150–200, 200–250 and 250–300 hPa. For these layers the MOZAIC statistics are the most plentiful. Only grid cells with statistics of more than one hundred measurements are kept. Both tropospheric and stratospheric data are used. We remind that ice supersaturation occurrence from AIRS represents the occurrence of supersaturation at any altitude within a pressure layer ("at least once" supersaturation occurrence). Therefore, it is important to determine ISS occurrence frequencies for MOZAIC in a similar manner. We use the same relative humidity threshold for the detection of ice supersaturation in the MOZAIC data as the one used to construct the S-function, that is to say $RHi_M > 100\,\%$ (lowered threshold to compensate for the fact that MOZAIC does not detect supersaturation at altitudes below or above flight altitude within the pressure layer boundaries, see Sect. 3.2). The ISS frequencies from MOZAIC are then slightly higher in our calculation than the one in Gierens et al. (2000). As Fig. 5 supports, it can be shown that the statistics using $RHi_M > 110\,\%$ over the period 2002–2007 are comparable to the statistics using $RHi_M > 100\,\%$ over the period 1995–1997.

Figure 12 presents maps of ISS occurrences from AIRS (left) and MOZAIC (right) for the years 2002–2007 and separately for the pressure layers 150–200, 200–250, and 250–300 hPa. For an easier comparison we mask the AIRS data corresponding to grid cells where MOZAIC data are available. Geographical patterns and magnitudes agree fairly well considering the limitations of spatial and temporal sampling by MOZAIC (Fig. 2 and Sect. 2.3). The differences are particularly apparent close to the tropopause and in regions with high seasonal variability (the Arctic for example) and/or small MOZAIC coverage. The AIRS climatology is

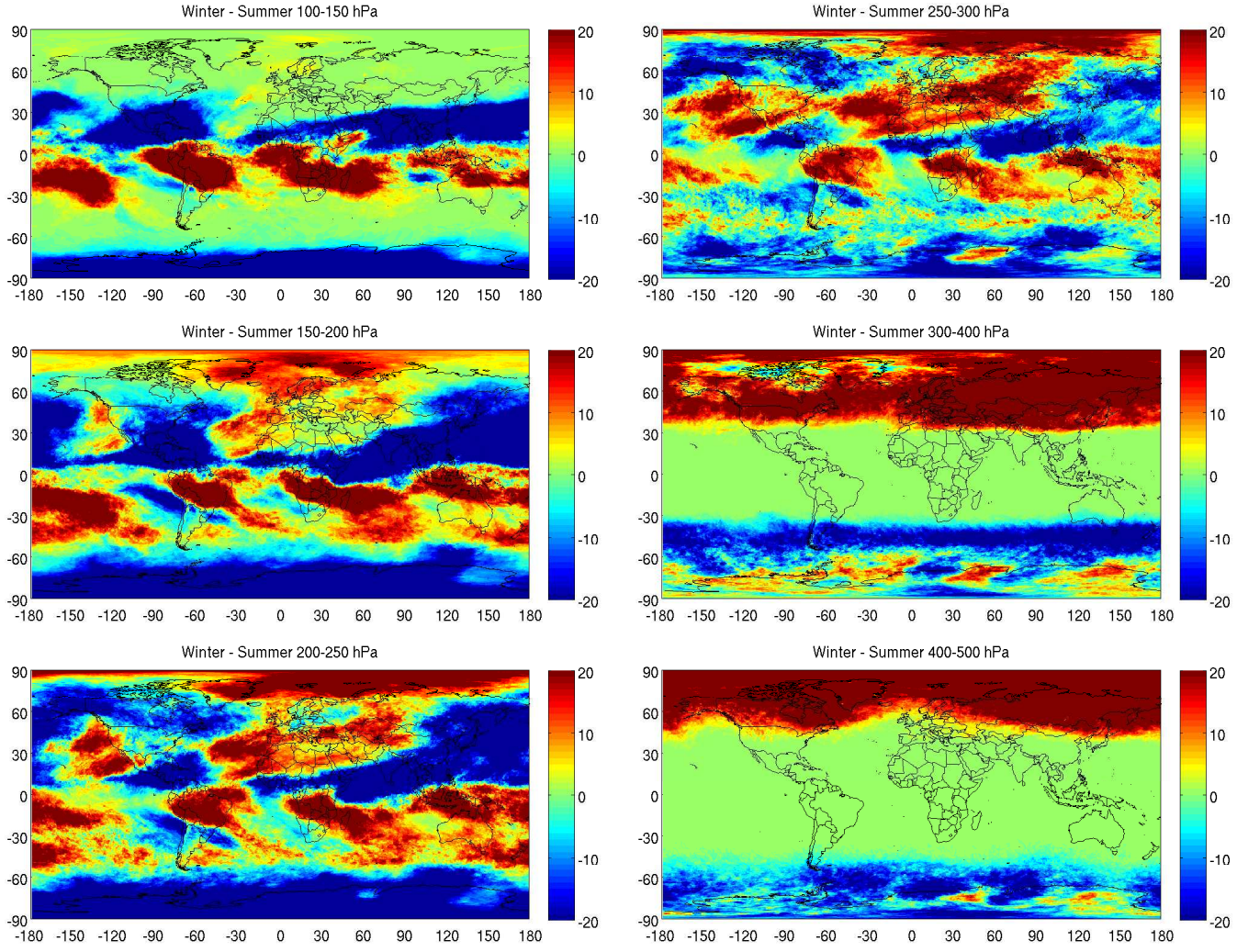

Fig. 16. Ice supersaturation occurrence frequencies (%) from ECMWF ("layer supersaturation" scheme) in the pressure layers 100–150, 150–200, 200–250, 250–300, 300–400 and 400–500 hPa. Boreal winter – boreal summer. Year 2007.

less noisy than MOZAIC because all seasons are equally well represented.

This comparison highlights the benefit of our method exploiting the synergy between AIRS and MOZAIC. We keep the best from these two datasets: the ability to detect thin supersaturated layers from MOZAIC and the global coverage from AIRS.

4.4 Relationship with cirrus occurrences from CALIOP

To relate ice supersaturation also to the very thinnest cirrus, we relate in this study AIRS ISS occurrence to occurrence of high clouds from CALIOP. CALIOP (Winker et al., 2003, 2007, 2009) is the first spaceborne lidar set for a long duration mission. The active lidar is able to detect also subvisible cirrus to which the IR sounders are not sensitive (Stubenrauch et al., 2010) and its vertical resolution is about 60 m in the upper troposphere. We recall that the analysis of a backscattered laser beam allows a vertical profiling of clouds having low optical depths (maximum about 5).

To relate ice supersaturation occurrence from AIRS to cloud occurrence from CALIOP we determine if a cloud occurs within the AIRS pressure layer. Since the lidar nadir geometry prohibits reaching very high latitudes statistics are therefore limited to latitudes between 80° N and 80° S. Figure 13 shows zonal means of cirrus occurrence, averaged over the period 2007–2008. It follows the ice supersaturation occurrence from AIRS in Fig. 11 (left) which indicates the cause-to-consequence relationship between ice supersaturation and cirrus clouds: ice clouds form where ice supersaturation takes place as the latter is a prerequisite for ice cloud formation.

In Gierens et al. (2000) correlations are shown between ice supersaturation occurrence from MOZAIC and occurrence of subvisible cirrus detected from the Stratospheric Aerosol and Gas Experiment (SAGE II Wang et al., 1996). For the

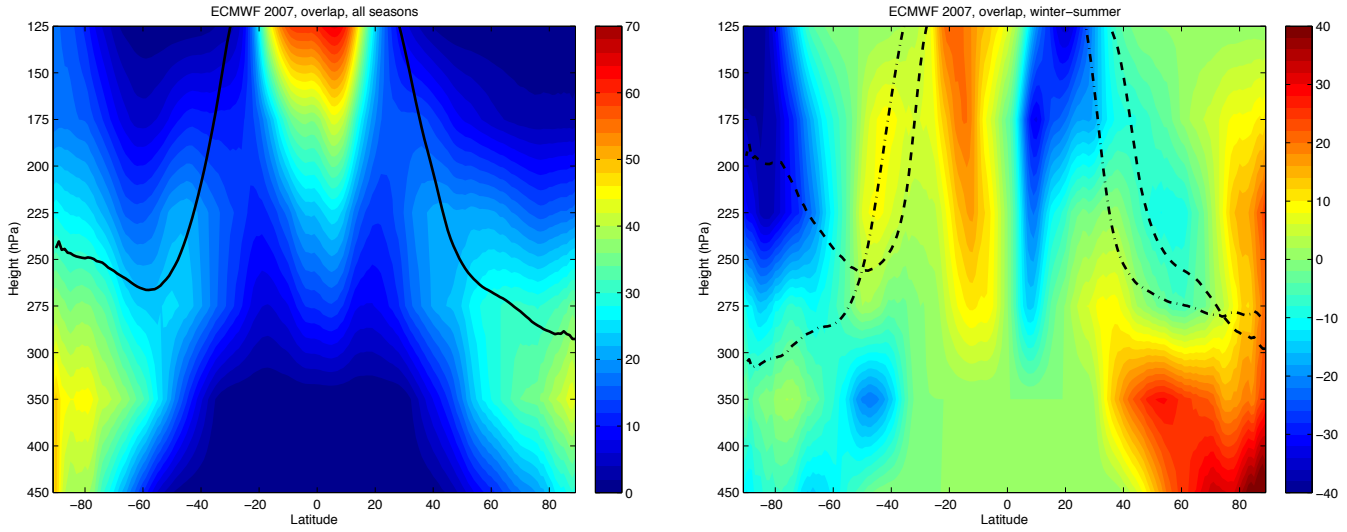

Fig. 17. Zonal means of ice supersaturation occurrence frequencies (%) from ECMWF ("layer supersaturation" scheme) for the year 2007 (left) along with boreal winter minus boreal summer differences (right). Plain line: zonal-mean tropopause (all seasons). Dashed line: zonal mean summer tropopause. Pointed dashed line: zonal mean winter tropopause.

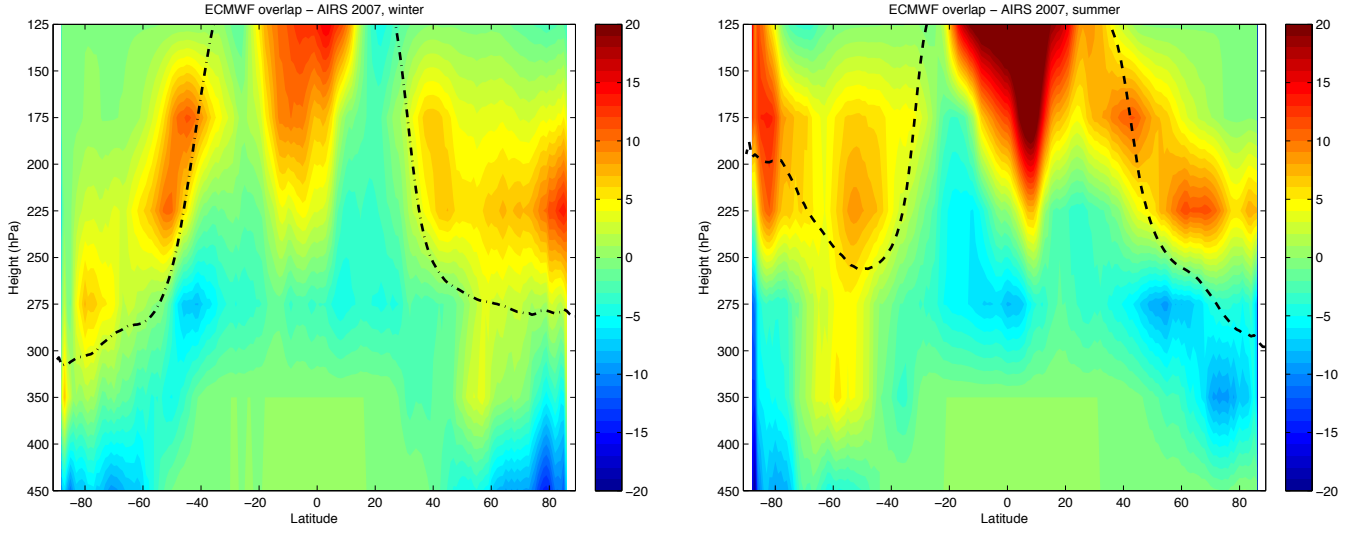

Fig. 18. Zonal means of ice supersaturation occurrence differences between ECMWF ("layer supersaturation" scheme) and AIRS for the 2007 boreal winter (left) and summer (right). Dashed line: zonal mean summer tropopause. Pointed dashed line: zonal mean winter tropopause.

first time we are able to extend this relationship to other regions and to optically thicker cirrus (up to an optical depth of 5). Figure 14 compares these relationships in the Northern Hemisphere and Southern Hemisphere (SH), separately in the tropics (0–30°), in the midlatitudes (30–60°) and in the polar regions (60–90°). Only the pressure layers below the tropopause are considered, with statistics of more than one hundred CALIOP measurements. Cirrus occurrence statistics and ice supersaturation statistics are determined for each season at a spatial resolution of 1° lat × 1° lon. The standard deviation in Fig. 14 indicates the seasonal and spatial variabilities as well as the sampling noise of the cirrus occurrences from CALIOP (about one track of 70 m every 1000 km). The uncertitudes are too large to detect differences between NH and SH, but one observes an increasing slope from polar regions towards the tropics, probably linked to different formation mechanisms.

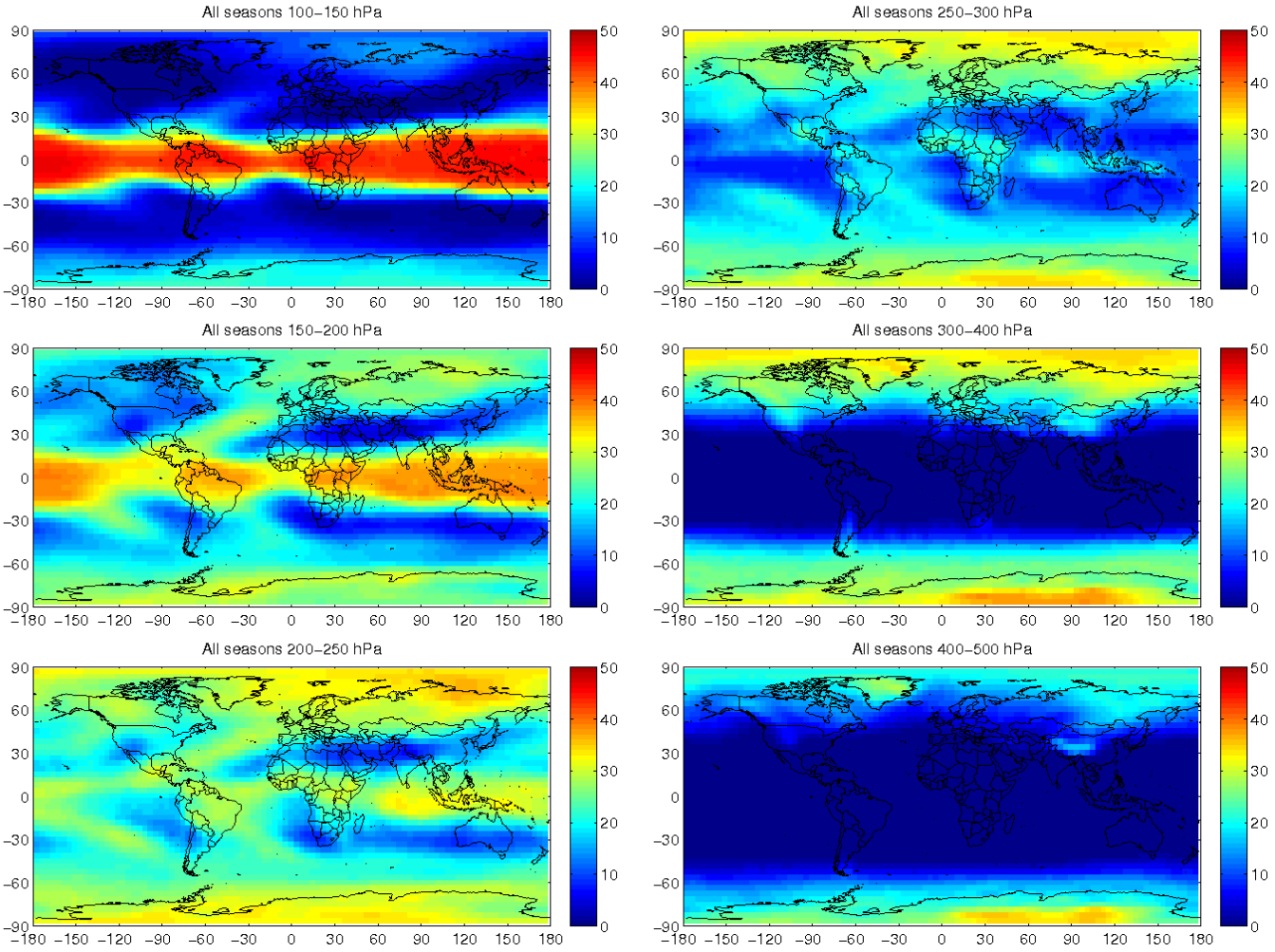

Fig. 19. Ice supersaturation occurrence frequencies (%) from ECHAM in the pressure layers 100–150, 150–200, 200–250, 250–300, 300–400 and 400–500 hPa. 5 yr of simulation.

5 Comparisons with ice supersaturation occurrences from ECMWF and ECHAM

In recent years, several global circulation models have included comprehensive ice supersaturation (e.g. Gettelman et al., 2010; Salzmann et al., 2010). The Integrated Forecast System (IFS) of the ECMWF (Tompkins et al., 2007) resolves supersaturation whereas the ECHAM4 climate model infers supersaturation from the cloud scheme (Burkhardt et al., 2008). Evaluations of ISS statistics with observations are required for potential improvements of ISS parametrizations (e.g. Lamquin et al., 2009; Rädel and Shine, 2010). In the following we compare global AIRS ISS occurrence frequencies to those derived from two different models: the ECMWF forecast model and the ECHAM4 climate model. In both datasets the same temperature criterion at the bottom of the layers is used as the one described in Sect. 4.2 and no emissivity threshold is yet applied to remove the thickest cirrus (see Sect. 2.2).

5.1 Comparison with ECMWF

Although AIRS radiances are assimilated in the ECMWF model (McNally et al., 2006) ice supersaturation, as derived from AIRS in this study, cannot be directly assimilated. Lamquin et al. (2009) compared upper tropospheric relative humidity from the IFS and from AIRS. No comparison of ice supersaturation occurrence was possible because a method to determine ISS occurrence within the relatively large pressure layers of AIRS had not yet been developed. We are now able to perform such a comparison.

For this purpose, high vertical resolution forecasts are extracted globally for the whole year 2007. They consist of 24 h-forecasts of relative humidity and temperature simulated at a spectral resolution of T799 (about 25 km at the equator) and 91 layers in the vertical (about 15 hPa). 24 h-forecasts are used rather than initial fields at 0-h lead time because of the spinup behaviour of ice supersaturation in the IFS (Lamquin et al., 2009).

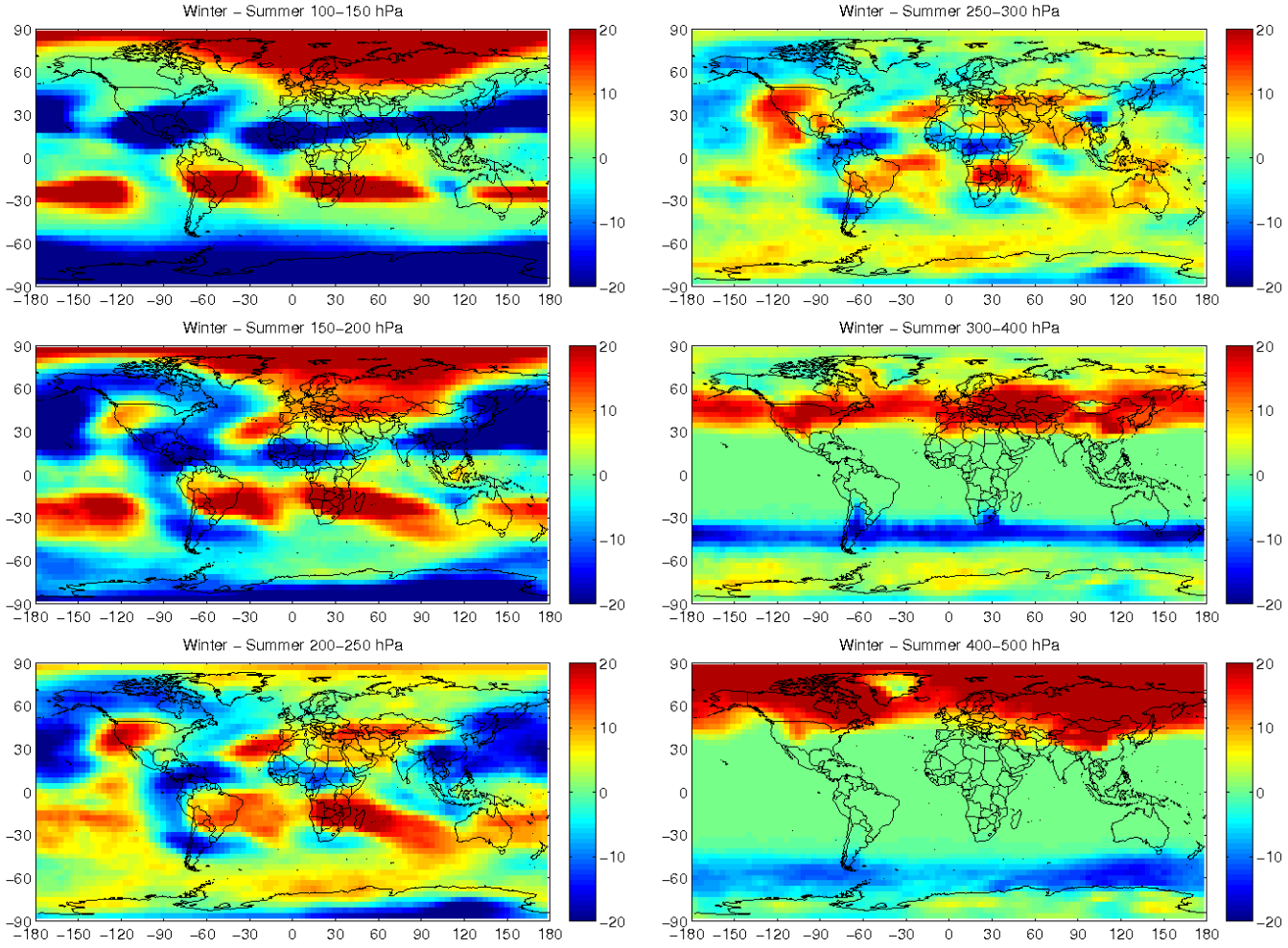

Fig. 20. Ice supersaturation occurrence frequencies (%) from ECHAM in the pressure layers 100–150, 150–200, 200–250, 250–300, 300–400 and 400–500 hPa. Boreal winter – boreal summer. 5 yr of simulation.

We extracted data in a regular $0.5 \times 0.5°$ grid with vertical levels spaced by 25 hPa between 100 and 500 hPa. For the comparison the ice supersaturation occurrence frequencies in the IFS are computed using a "layer supersaturation" (or "overlap") scheme declaring ice supersaturation present within one pressure layer (e.g. 200–250 hPa) when any of the vertical levels of this layer exhibits ice supersaturation (in this case: 200, 225 or 250 hPa).

Figures 15 and 16 first present climatologies of ISS occurrence frequencies from the IFS and its difference between boreal winter and summer for the year 2007. Even though the AIRS climatology covers 7 yr Figs. 15 and 16 show a good correspondence with the geographical patterns and magnitudes seen in Figs. 9 and 10. However, for the IFS, Fig. 15 shows slightly higher frequencies in the tropics and in the regions of the storm tracks and jet streams which is consistent with an underestimation of ISS occurrences from AIRS over regions with a high amount of thick cirrus.

For a closer comparison Fig. 17 shows, for the year 2007 for both datasets, the zonal means of ISS occurrence frequencies (left) along with the boreal winter minus summer differences (right). In addition, Fig. 18 shows, for the year 2007, the zonal means of the differences between the IFS and AIRS where we have separated boreal winter (left) and boreal summer (right).

In the tropical regions the comparisons above 200 hPa indicate the importance of the a priori used to retrieve the whole AIRS profile. Indeed, absolute values, seasonal differences and values relative to AIRS show the most disagreement in this region. In the other regions both the zonal means and the seasonal differences in Fig. 17 show remarkable similarities with the ones from AIRS in Fig. 11. However, a possible effect of the "layer supersaturation" scheme is supersaturation extending slightly higher above the tropopause than for AIRS. In Fig. 18, with the exception of the regions of the storm tracks and jet streams, the crossing of the extratropical tropopause inverts the sign of the difference between

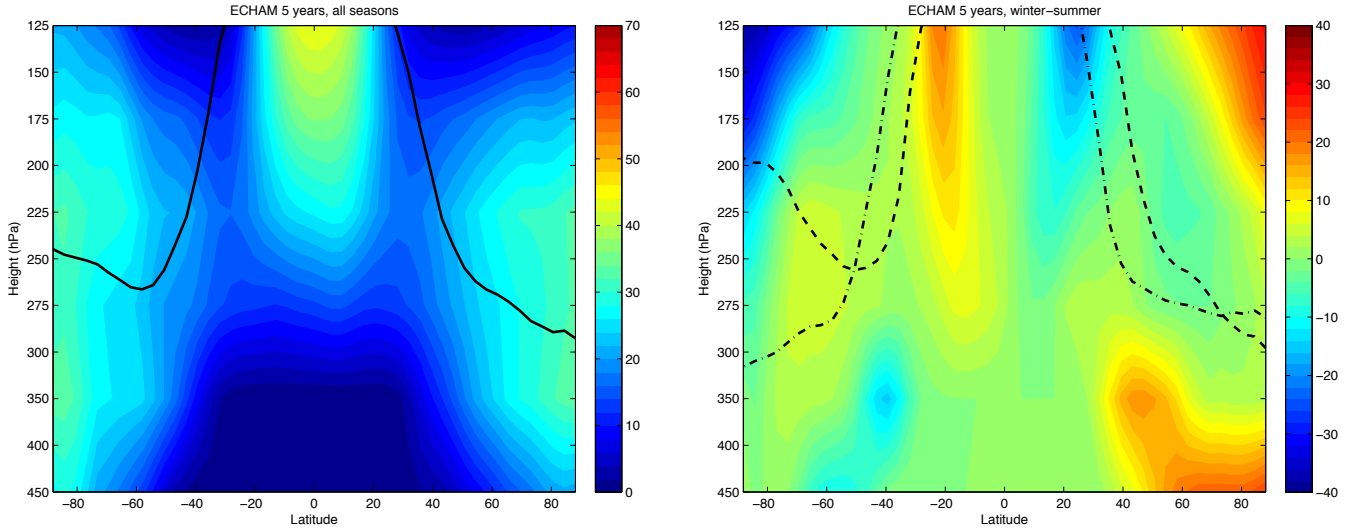

Fig. 21. Zonal means of ice supersaturation occurrence frequencies (%) from ECHAM (5 yr of simulation) (left) along with boreal winter minus boreal summer differences (right). Plain line: zonal-mean tropopause (all seasons). Dashed line: zonal mean summer tropopause. Pointed dashed line: zonal mean winter tropopause.

the IFS zonal means and the AIRS zonal means (AIRS higher below, IFS higher above).

5.2 Comparison with ECHAM

In the ECHAM4 climate model (Röckner et al., 1996) ice supersaturation frequency has been parameterized consistently with the cloud scheme (Burkhardt et al., 2008) in order to enable the simulation of the climate effect of contrail cirrus (Burkhardt et al., 2009). The parameterization uses the information on subgrid scale variability of relative humidity that is inherent in the parameterization of fractional cloud coverage and infers a fractional supersaturated area. The model has been run with a T30/L39 resolution for 5 yr and we compare the resulting climatology with observations. Vertical levels were spaced between 100 and 200 hPa by 15 hPa and the spacing increased slowly to 30 hPa between 400 and 500 hPa.

Due to the coarse horizontal resolution of the model we calculate the fractional supersaturated area at each level within a pressure layer. We then apply a maximum random overlap scheme (as used in the cloud scheme) in order to calculate the fractional supersaturated area for a specified layer.

Ice supersaturation occurrence is then assessed globally in the same pressure layers 100–150, 150–200, 200–250, 250–300, 300–400, 400–500 hPa at the ECHAM spatial resolution of 3.75° lat ×3.75° lon. Figures 19 and 20 show respectively the global occurrences of ice supersaturation over the 5 yr of simulation and the difference between boreal winter and summer.

Despite the low resolution of the climate model the geographical patterns and absolute values of supersaturation are quite well represented. The most obvious deficiency is that in the 150–200 hPa and the 200–250 hPa layers the climate model overestimates supersaturation frequency in the extratropics. This is due to the fact that the model's tropopause is too high in the extratropics so that those layers are too frequently part of the troposphere. The bias in tropopause height is connected with the model's lower stratospheric cold bias, a common problem in climate models (particularly at low resolution).

As for the IFS, Figs. 21 and 22 show zonal means of ISS occurrence frequencies, seasonal differences and comparisons to AIRS. The zonal means as well as their seasonal differences in Fig. 21 are consistent with AIRS in Fig. 11 with however much smaller values and differences at the highest latitudes, the seasonal cycle is well represented. The impact of the bias in tropopause height is obvious with ECHAM supersaturation extending very high above the mean tropopause. Also, ECHAM is unable to reproduce the rise in ISS at 40–50° S that is connected with the SH storm tracks.

6 Conclusions

We have presented a climatology of ice supersaturation occurrence from AIRS observations covering the period 2003–2009. The relatively coarse vertical resolution of the AIRS retrieved water vapour profiles prohibits the direct detection of shallow supersaturated layers. Therefore, we have developed a calibration method for the detection of ice supersaturation by AIRS: space and time collocations of the detection of ice supersaturation by MOZAIC with coarsely-determined relative humidity profiles from AIRS allows the determination of an a priori probability function (the "S-function")

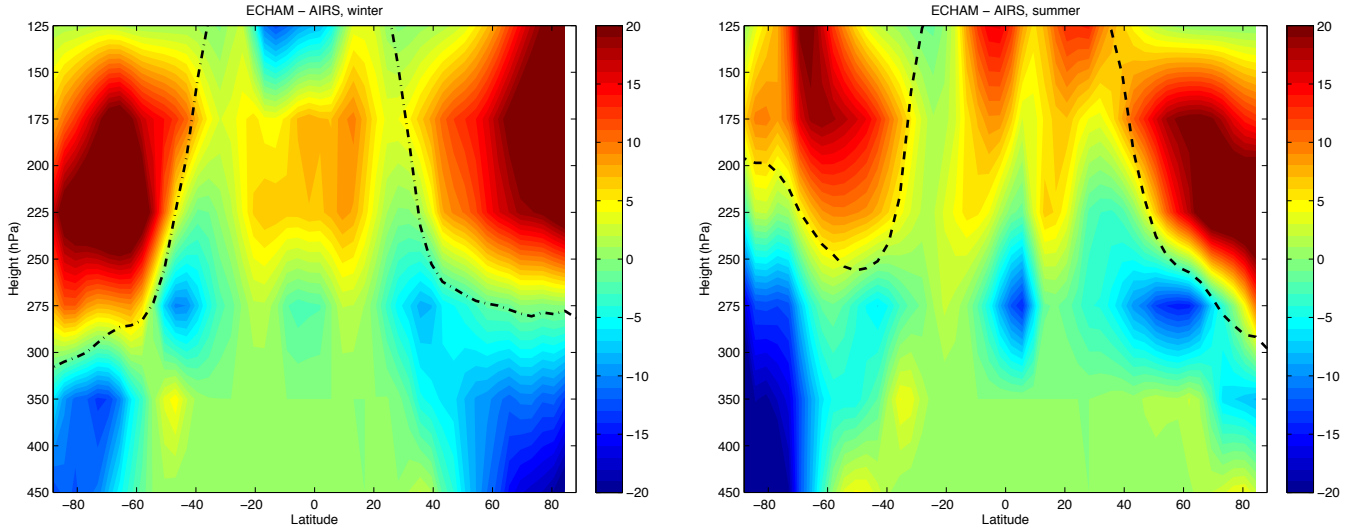

Fig. 22. Zonal means of ice supersaturation occurrence differences between ECHAM and AIRS (left) for the boreal winter (left) and summer (right). Dashed line: zonal mean summer tropopause. Pointed dashed line: zonal mean winter tropopause.

of ice supersaturation occurrence for any relative humidity value determined by AIRS.

We have used the S-function to establish a climatology of ice supersaturation occurrence over the whole upper troposphere. The horizontal extent of ice supersaturation is an important feature for large-scale model parameterization, an evaluation of it is presented by use of a simple cluster analysis. Due to the lower reliability of AIRS data at high altitudes we raise caution on our results in pressure layers 100–150 and 150–200 hPa. The ISS statistics represent the probability that ice supersaturation occurs at least once within a given pressure layer and therefore show higher values than previous published works using a threshold of 100 % on RHi. It compares relatively well to other pre-existing climatologies with high supersaturation occurrences near the tropical tropopause, in the region of the storm tracks and jet streams in the midlatitudes and close to the Arctic tropopause with a concomitant seasonal cycle. An evaluation of the climatology is presented with statistics from MOZAIC only; it shows the benefit obtained from the synergy between AIRS and MOZAIC. Relationships with cirrus cloud statistics from CALIOP shows the cause-to-consequence link between ice supersaturation and cirrus cloud formation: cirrus clouds form where ice supersaturation takes place.

As possible applications, we compare the AIRS climatology to model climatologies from ECMWF 24 h-forecasts and ECHAM4 between 100 and 500 hPa. Except close to the tropical tropopause where AIRS has much higher uncertainties and in regions with possible influence of the tropopause lying within pressure layers, the comparison with the ECMWF forecasts shows corresponding values and patterns globally and seasonally. The climatology from ECHAM4 has a lower horizontal resolution and therefore exhibits a smaller variability than AIRS and ECMWF. Nevertheless, it captures the main patterns of ISS successfully in the upper troposphere. The main deficiency being the bias in tropopause height which is connected with the model's lower stratospheric cold bias.

Overall, this paper presents a way of dealing with the difficulty of remotely sensing ice supersaturation and comparing statistics from various observations and models. We propose a bridge between those different means of investigation by the use of the synergy between infrared sounding and in situ measurements. Among future applications of this work a climatology of potential condensation trails from aircraft will be assessed. For more detailed studies it would be first necessary to remove optically thick cirrus in the climate models to be more close to the observations. It would also be interesting to investigate if the relationships between occurrence of cirrus and of ISS observed by CALIPSO and AIRS can be reproduced by the models.

Supplementary material related to this article is available online at: http://www.atmos-chem-phys.net/12/381/2012/acp-12-381-2012-supplement.pdf.

Acknowledgements. This work was supported by CNRS and Ecole Polytechnique. The AIRS version 5 data were obtained through the Goddard Earth Sciences Data and Information Services (http://daac.gsfc.nasa.gov/) and the CALIOP data were obtained through the Atmospheric Sciences Data Center (ASDC) at NASA Langley Research Center by the ICARE Thematic Center created by CNES (http://www-icare.univ-lille1.fr/) and its interface ClimServ created for Institut Pierre-Simon Laplace (http://climserv.ipsl.polytechnique.fr/). The authors acknowledge for the strong support of the European Commission, Airbus, and

the Airlines (Lufthansa, Austrian, Air France) who carry free of charge the MOZAIC equipment and perform the maintenance since 1994. MOZAIC is presently funded by INSU-CNRS (France), Meteo-France, and Forschungszentrum (FZJ, Julich, Germany). The MOZAIC data base is supported by ETHER (CNES and INSU-CNRS). ECMWF data have been retrieved within the framework of a special project on "Ice Supersaturation and Cirrus Clouds (SPDEISSR)". The authors thank all the corresponding teams for assistance and public release of data products. The work contributes to COST Action ES-0604 "Water Vapour in the Climate System (WaVaCS)" and to the aforementioned SPDEISSR. The authors thank the reviewers for their fruitful comments.

Edited by: T. J. Dunkerton

The publication of this article is financed by CNRS-INSU.

References

Burkhardt, U., Kärcher, B., Ponater, M., Gierens, K., and Gettelman, A.: Contrail cirrus supporting areas in model and observations, Geophys. Res. Lett., 35, L16808, doi:10.1029/2008GL034056, 2008.

Burkhardt, U. and Kärcher, B.: Process-based simulation of contrail cirrus in a global climate model, J. Geophys. Res., 114, D16201, doi:10.1029/2008JD011491, 2009.

Chahine, M. T., Pagano, T. S., Aumann, H. H., et al.: AIRS: Improving weather forecasting and providing new data on greenhouse gases, B. Am. Meteorol. Soc., 87, 911–926, 2006.

Dickson, N. C., Gierens, K. M., Rogers, H. L., and Jones, R. L.: Probabilistic description of ice-supersaturated layers in low resolution profiles of relative humidity, Atmos. Chem. Phys., 10, 6749–6763, doi:10.5194/acp-10-6749-2010, 2010.

Divakarla, M. G., Barnet, C. D., Goldberg, M. D., McMillin, L. M., Maddy, E., Wolf, W., Zhou, L., and Liu, X.: Validation of Atmospheric Infrared Sounder temperature and water vapour retrievals with matched radiosondes measurements and forecasts, J. Geophys. Res., 111, D09S15, doi:10.1029/2005JD006116, 2006.

Fetzer, E. J., Read, W. G., Waliser, D., Kahn, B. H., Tian, B., Vömel, H., Irion, F. W., Su, H., Eldering, A., de la Torre Juarez, M., Jiang, J., and Dang, V.: Comparison of upper tropospheric water vapor observations from the Microwave Limb Sounder and Atmospheric Infrared Sounder, J. Geophys. Res., 113, D22110, doi:10.1029/2008JD010000, 2008.

Gettelman, A., Weinstock, E. M., Fetzer, E. J., Irion, F. W., Eldering, A., Richard, E. C., Rosenlof, K. H., Thompson, T. L., Pittman, J. V., Webster, C. R., and Herman, R. L.: Validation of Aqua satellite data in the upper troposphere and lower stratosphere with in situ aircraft instruments, Geophys. Res. Lett., 31, L22107, doi:10.1029/2004GL020730, 2004.

Gettelman, A., Fetzer, E. J., Eldering, A., and Irion, F. W.: The global distribution of supersaturation in the upper troposphere from the Atmospheric Infrared Sounder, J. Climate, 19, 6089–6103, 2006a.

Gettelman, A., Walden, V. P., Miloshevich, L. M., Roth, W. L., and Halter, B.: Relative humidity over Antarctica from radiosondes, satellites, and a general circulation model, J. Geophys. Res., 111, D09S13, doi:10.1029/2005JD006636, 2006b.

Gettelman, A., Liu, X., Ghan, S. J., Morrison, H., Park, S., Conley, A. J., Klein, S. A., Boyle, J., Mitchell, D. L., and Li, J.-L. F.: Global simulations of ice nucleation and ice supersaturation with an improved cloud scheme in the community atmosphere model, J. Geophys. Res., 115, D18216, doi:10.1029/2009JD013797, 2010.

Gierens, K.: Are fuel additives a viable contrail mitigation option?, Atmos. Environ., 41, 4548–4552, doi:10.1016/j.atmosenv.2007.03.014, 2007.

Gierens, K. and Brinkop, S.: A model for the horizontal exchange between ice-supersaturated regions and their surrounding area, Theor. Appl. Climatol., 71, 129–140, 2002.

Gierens, K. and Spichtinger, P.: On the size distribution of ice-supersaturated regions in the upper troposphere and lowermost stratosphere, Ann. Geophys., 18, 499–504, doi:10.1007/s00585-000-0499-7, 2000.

Gierens, K., Schumann, U., Helten, M., Smit, H., and Marenco, A.: A distribution law for relative humidity in the upper troposphere and lower stratosphere derived from three years of MOZAIC measurements, Ann. Geophys., 17, 1218–1226, doi:10.1007/s00585-999-1218-7, 1999.

Gierens, K., Schumann, U., Helten, M., Smit, H. and Wang, P.-H.: Ice-supersaturated regions and subvisible cirrus in the northern midlatitudes upper troposphere, J. Geophys. Res., 105, 22743–22753, 2000.

Gierens, K., Kohlhepp, R., Spichtinger, P., and Schroedter-Homscheidt, M.: Ice supersaturation as seen from TOVS, Atmos. Chem. Phys., 4, 539–547, doi:10.5194/acp-4-539-2004, 2004.

Haag, W., Kärcher, B., Ström, J., Minikin, A., Lohmann, U., Ovarlez, J., and Stohl, A.: Freezing thresholds and cirrus cloud formation mechanisms inferred from in situ measurements of relative humidity, Atmos. Chem. Phys., 3, 1791–1806, doi:10.5194/acp-3-1791-2003, 2003.

Immler, F., Treffeisen, R., Engelbart, D., Krüger, K., and Schrems, O.: Cirrus, contrails, and ice supersaturated regions in high pressure systems at northern mid latitudes, Atmos. Chem. Phys., 8, 1689–1699, doi:10.5194/acp-8-1689-2008, 2008.

Jensen, E. J., Smith, J. B., Pfister, L., Pittman, J. V., Weinstock, E. M., Sayres, D. S., Herman, R. L., Troy, R. F., Rosenlof, K., Thompson, T. L., Fridlind, A. M., Hudson, P. K., Cziczo, D. J., Heymsfield, A. J., Schmitt, C., and Wilson, J. C.: Ice supersaturations exceeding 100 % at the cold tropical tropopause: implications for cirrus formation and dehydration, Atmos. Chem. Phys., 5, 851–862, doi:10.5194/acp-5-851-2005, 2005.

Kahn, B. H., Liang, C. K., Eldering, A., Gettelman, A., Yue, Q., and Liou, K. N.: Tropical thin cirrus and relative humidity observed by the Atmospheric Infrared Sounder, Atmos. Chem. Phys., 8, 1501–1518, doi:10.5194/acp-8-1501-2008, 2008.

Kahn, B. H., Gettelman, A., Fetzer, E. J., Eldering, A., and Liang, C. K.: Cloudy and clear sky relative humidity in the upper troposphere observed by the A-train, J. Geophys. Res., 114, D00H02,

doi:10.1029/2009JD011738, 2009.

Kärcher, B. and Lohmann, U.: A parametrization of cirrus cloud formation: Homogeneous freezing of supercooled aerosols, J. Geophys. Res., 107, 4010, doi:10.1029/2001JD000470, 2002.

Krämer, M., Schiller, C., Afchine, A., Bauer, R., Gensch, I., Mangold, A., Schlicht, S., Spelten, N., Sitnikov, N., Borrmann, S., de Reus, M., and Spichtinger, P.: Ice supersaturations and cirrus cloud crystal numbers, Atmos. Chem. Phys., 9, 3505–3522, doi:10.5194/acp-9-3505-2009, 2009.

Lamquin, N., Stubenrauch, C. J., and Pelon, J.: Upper tropospheric humidity and cirrus geometrical and optical thickness: relationships inferred from one year of collocated AIRS-CALIPSO data, J. Geophys. Res., 113, D00A08, doi:10.1029/2008JD010012, 2008.

Lamquin, N., Gierens, K., Stubenrauch, C. J., and Chatterjee, R.: Evaluation of upper tropospheric humidity forecasts from ECMWF using AIRS and CALIPSO data, Atmos. Chem. Phys., 9, 1779–1793, doi:10.5194/acp-9-1779-2009, 2009.

Leiterer, U., Dier, H., Nagel, D., Naebert, T., Althausen, D., Franke, K., Kats, A., and Wagner, F.: Correction method for RS80 A-Humicap humidity profiles and their validation by Lidar backscattering profiles in tropical cirrus clouds, J. Atmos. Ocean. Tech., 22, 18–29, 2005.

Liang, C. K., Eldering, A., Gettelman, A., Tian, B., Wong, S., Fetzer, E. J., and Liou, K. N.: Record of tropical interannual variability of temperature and water vapor from a combined AIRS-MLS data set, J. Geophys. Res., 116, D06103, doi:10.1029/2010JD014841, 2011.

Luo, Z., Kley, D., Johnson, R. H., and Smit, H. G. J.: Ten years of measurements of tropical upper-tropospheric water vapor by MOZAIC. Part II: assessing the ECMWF humidity analysis, J. Climate, 21, 1449–1466, 2007.

Mace, G. G., Zhang, Q., Vaughan, M., Marchand, R., Stephens, G., Trepte, C., and Winker, D.: A description of hydrometeor layer occurrence statistics derived from the first year of merged Cloudsat and CALIPSO data, J. Geophys. Res., 114, D00A26, doi:10.1029/2007JD009755, 2009.

Maddy, E. S. and Barnet, C. D.: Vertical resolution estimates in Version 5 of AIRS operational retrievals, IEEE T. Geosci. Remote Sens., 46, 2375–2384, 2008.

Marquart, S., Ponater, M., Mager, F., and Sausen, R.: Future Development of Contrail Cover, Optical Depth, and Radiative Forcing: Impacts of Increasing Air Traffic and Climate Change, J. Climate, 16, 2890–2904, 2003.

Marenco, A., Thouret, V., Nédélec, P., Smit, H. G., Helten, M., Kley, D., Karcher, F., Simon, P. , Law, K., Pyle, J., Poschmann, G., Von Wrede, R., Hume, C., and Cook, T.: Measurements of ozone and water vapour by in-service Airbus aircraft: the MOZAIC airborne program, an overview, J. Geophys. Res., 103, 25631–25642, 1998.

McNally, A. P., Watts, P. D., Smith, J. A., Engelen, R., Kelly, G. A., Thépaut, J. N., and Matricardi, M.: The assimilation of AIRS radiance data at ECMWF, Q. J. Roy. Meteor. Soc., 132, 935–957, 2006.

Montoux, N., Hauchecorne, A., Pommereau, J.-P., Lefèvre, F., Durry, G., Jones, R. L., Rozanov, A., Dhomse, S., Burrows, J. P., Morel, B., and Bencherif, H.: Evaluation of balloon and satellite water vapour measurements in the Southern tropical and subtropical UTLS during the HIBISCUS campaign, Atmos. Chem. Phys., 9, 5299–5319, doi:10.5194/acp-9-5299-2009, 2009.

Ovarlez, J., Gayet, J.-F., Gierens, K., Ström, J., Ovarlez, H., Auriol, F., Busen, R., and Schumann, U.: Water vapor measurements inside cirrus clouds in northern and southern hemispheres during INCA, Geophys. Res. Lett., 29, 1813, doi:10.1029/2001GL014440, 2002.

Peirce, C.: The numerical measure of the success of predictions, Science, 12, 453–454, 1884.

Pruppacher, H. R.: A new look at homogeneous ice nucleation in supercooled water drops, J. Atmos. Sci., 52, 1924–1933, 1994.

Rädel, G. and Shine, K. P.: Evaluation of the use of radiosonde humidity data to predict the occurrence of persistent contrails, Q. J. Roy. Meteor. Soc., 133, 1413–1423, 2007.

Rädel, G. and Shine, K. P.: Radiative forcing by persistent contrails and its dependence on cruise altitudes, J. Geophys. Res., 113, D07105, doi:10.1029/2007JD009117, 2008.

Rädel, G. and Shine, K. P.: Validating ECMWF forecasts for the occurrence of ice supersaturation using visual observations of persistent contrails and radiosonde measurements over England, Q. J. Roy. Meteor. Soc, 136, 1723–1732, doi:10.1002/qj.670, 2010.

Read, W. G., Lambert, A., Bacmeister, J., et al.: Aura Microwave Limb Sounder upper tropospheric and lower stratospheric H_2O and relative humidity with respect to ice validation, J. Geophys. Res., 112, D24S35, doi:10.1029/2007JD008752, 2007.

Röckner, E., Arpe, K., Bengtsson, L., Christoph, M., Claussen, M., Dümenil, L., Esch, M., Giorgetta, M., Schlese, U., and Schulzweida, U.: The atmosphere general circulation model ECHAM-4: Model description and simulation of present-day climate, Max-Planck-Inst. Meteorol. Rep. 218, 90 pp., Hamburg, Germany, 1996.

Salzmann, M., Ming, Y., Golaz, J.-C., Ginoux, P. A., Morrison, H., Gettelman, A., Krämer, M., and Donner, L. J.: Two-moment bulk stratiform cloud microphysics in the GFDL AM3 GCM: description, evaluation, and sensitivity tests, Atmos. Chem. Phys., 10, 8037–8064, doi:10.5194/acp-10-8037-2010, 2010.

Sassen, K. and Wang, Z.: Classifying clouds around the globe with CloudSat radar: 1-year of results, Geophys. Res. Let., 45, L04805, doi:10.1029/2007GL032591, 2008.

Schumann, U.: On conditions for contrail formation from aircraft exhausts, Meteorol. Z., 5, 4–23, 1996.

Soden, B. J. and Lanzante, J. R.: An assessment of satellite and radiosonde climatologies of upper-tropospheric water vapor, J. Climate, 9, 1235–1250, 1996.

Sonntag, D.: Important new values of the physical constants of 1986, vapor pressure formulation based on the ITS-90 and psychrometer formulae, Meteorol. Z., 70, 340–344, 1990.

Spichtinger, P. and Gierens, K. M.: Modelling of cirrus clouds – Part 1a: Model description and validation, Atmos. Chem. Phys., 9, 685–706, doi:10.5194/acp-9-685-2009, 2009a.

Spichtinger, P. and Gierens, K. M.: Modelling of cirrus clouds – Part 1b: Structuring cirrus clouds by dynamics, Atmos. Chem. Phys., 9, 707–719, doi:10.5194/acp-9-707-2009, 2009b.

Spichtinger, P., Gierens, K., Leiterer, U., and Dier, H.: Ice supersaturation in the tropopause region over Lindenberg, Germany, Meteorol. Z., 12, 143–156, 2003a.

Spichtinger, P., Gierens, K., and Read, W.: The global distribution of ice-supersaturated regions as seen by the Microwave Limb Sounder, Q. J. Roy. Meteor. Soc., 129, 3391–3410, 2003b.

Spichtinger, P., Gierens, K., Smit, H. G. J., Ovarlez, J., and Gayet,

J.-F.: On the distribution of relative humidity in cirrus clouds, Atmos. Chem. Phys., 4, 639–647, doi:10.5194/acp-4-639-2004, 2004.

Stephens, G., Vane, D. G., Boain, R. J., et al.: The CloudSat mission and the A-train, B. Am. Meteorol. Soc., 83, 1771–1790, 2002.

Stubenrauch, C. J. and Schumann, U.: Impact of air traffic on cirrus coverage, Geophys. Res. Lett., 32, L14813, doi:10.1029/2005GL022707, 2005.

Stubenrauch, C. J., Rossow, W. B., Scott, N. A., and Chédin, A.: Clouds as Seen by Satellite Sounders (3I) and Imagers (ISCCP): III) Combining 3I and ISCCP cloud parameters for better understanding of cloud radiative effects, J. Climate, 12, 3419–3442, 1999.

Stubenrauch, C. J., Cros, S., Lamquin, N., Armante, R., Chédin, A., Crevoisier, C., and Scott, N. A.: Cloud properties from AIRS and evaluation with CALIPSO, J. Geophys. Res, 113, D00A10, doi:10.1029/2008JD009928, 2008.

Stubenrauch, C. J., Cros, S., Guignard, A., and Lamquin, N.: A 6-year global cloud climatology from the Atmospheric InfraRed Sounder AIRS and a statistical analysis in synergy with CALIPSO and CloudSat, Atmos. Chem. Phys., 10, 7197–7214, doi:10.5194/acp-10-7197-2010, 2010.

Susskind, J., Barnet, C., and Blaisdell, J.: Retrieval of atmospheric and surface parameters from AIRS/AMSU/HSB data in the presence of clouds, IEEE T. Geosci. Remote Sens., 41, 390–409, 2003.

Susskind, J., Barnet, C., Blaisdell, J., Iredell, L., Keita, F., Kouvaris, L., Molnar, G., and Chahine, M.: Accuracy of geophysical parameters derived from AIRS/AMSU as a function of fractional cloud cover, J. Geophys. Res., 111, D09S17, doi:10.1029/2005JD006272, 2006.

Tobin, D. C., Revercomb, H. E., Knuteson, R. O., Lesht, B. M., Strow, L. L., Hannon, S. E., Feltz, W. F., Moy, L. A., Fetzer, E. J., and Cress, T. S.: Atmospheric radiation measurement site atmospheric state best estimates for Atmospheric Infrared Sounder temperature and water vapor retrieval validation, J. Geophys. Res., 111, D09S14, doi:10.1029/2005JD006103, 2006.

Tompkins, A. M., Gierens, K., and Rädel, G.: Ice supersaturation in the ECMWF Integrated Forecast System, Q. J. Roy. Meteor. Soc., 133, 53–63, 2007.

Treffeisen, R., Krejci, R., Ström, J., Engvall, A. C., Herber, A., and Thomason, L.: Humidity observations in the Arctic troposphere over Ny-Ålesund, Svalbard based on 15 years of radiosonde data, Atmos. Chem. Phys., 7, 2721–2732, doi:10.5194/acp-7-2721-2007, 2007.

Waliser, D. E., Li, J.-L. F., Woods, C. P., et al.: Cloud ice: A climate model challenge with signs and expectations of progress, J. Geophys. Res., 114, D00A21, doi:10.1029/2008JD010015, 2009.

Wang, P.-H., Minnis, P., McCormick, P., Kent, G. S., and Skeens, K. M.: A 6-year climatology of cloud occurrence frequency from Stratospheric Aerosol and Gas Experiment II observations (1985–1990), J. Geophys. Res., 101, 29407–29429, 1996.

Winker, D. M., Pelon, J., and McCormick, M. P.: The CALIPSO mission: Spaceborne lidar for observation of aerosols and clouds, Proc. SPIE, 4893, 1–11, 2003.

Winker, D. M., Hunt, W. H., and McGill, M. J.: Initial performance assessment of CALIOP, Geophys. Res. Lett., 34, L19803, doi:10.1029/2007GL030135, 2007.

Winker, D. M., Vaughan, M. A., Omar, A., Hu, Y., and Powell, K. A.: Overview of the CALIPSO mission and CALIOP data processing algorithms, J. Atmos. Ocean. Tech., 26, 2310–2323, 2009.